



Bar and hinge models for scalable analysis of origami[☆]



E.T. Filipov^a, K. Liu^b, T. Tachi^c, M. Schenk^d, G.H. Paulino^{b,*}

^a Department of Civil and Environmental Engineering, University of Michigan, Ann Arbor, MI 48109, USA

^b School of Civil and Environmental Engineering, Georgia Institute of Technology, Atlanta, GA 30332, USA

^c Graduate School of Arts and Sciences, University of Tokyo, Tokyo 153-8902, Japan

^d Department of Aerospace Engineering, University of Bristol, Bristol, UK

ARTICLE INFO

Article history:

Received 14 January 2017

Revised 24 April 2017

Available online 12 June 2017

Keywords:

Origami analysis

Bar and hinge model

Scalable model

Analysis of thin sheet structures

ABSTRACT

Thin sheets assembled into three dimensional folding origami can have various applications from reconfigurable architectural structures to metamaterials with tunable properties. Simulating the elastic stiffness and estimating deformed shapes of these systems is important for conceptualizing and designing practical engineering structures. In this paper, we improve, verify, and test a simplified bar and hinge model that can simulate essential behaviors of origami. The model simulates three distinct behaviors: stretching and shearing of thin sheet panels; bending of the initially flat panels; and bending along prescribed fold lines. The model is simple and efficient, yet it can provide realistic representation of stiffness characteristics and deformed shapes of origami structures. The simplicity of this model makes it well suited for the origami engineering community, and its efficiency makes it suitable for design problems such as optimization and parameterization of geometric origami variations.

© 2017 Elsevier Ltd. All rights reserved.

1. Introduction

The field of *origami* has grown in the past years as it offers novel solutions to problems in both science and engineering. Early applications took advantage of the idea that a system can be folded compactly and subsequently deployed, or that self-assembly can be used to construct a three dimensional structure by starting from a thin sheet. More recently, the community has harnessed the capability of folding to create adaptable systems and metamaterials that can be tuned through reconfigurations. Practical applications of origami engineering can range in scale from an architectural façade that can reconfigure to control shading at a large scale (Del Grosso and Basso, 2010) to the folding of DNA to create nano-scale mechanisms (Marras et al., 2015). As the field of origami has grown, so have the theoretical, analytical, and fabrication techniques that allow for the successful simulation and implementation of novel folding solutions.

The behavior and functionality of origami is influenced by the geometry of the fold pattern and the material properties. A typical origami consists of flat thin sheet *panels* (or facets) that are interconnected by *fold lines* (or hinges). An origami where deformation occurs only at the fold lines while keeping the panels

flat is called *rigid foldable*. Such a structure can undergo a continuous kinematic folding motion. Some origami can also be *flat foldable*, where the structure can fold into a two dimensional flat state, allowing for compact stowage. Origami structures can have high stiffness (Miura, 1972), multi-stability (Guest and Pellegrino, 1994), and stiffness against non-kinematic deformations (Schenk and Guest, 2011), which are behaviors governed by the geometry of the origami patterns, as well as the elastic properties of panels.

Characterizing the elastic behavior of origami has become important not only for evaluating the feasibility of origami as structural systems, but also for designing origami and analyzing non-trivial behaviors. The physics of origami are often a nonlinear coupling of folding motion along with both small and large deformations of panels (Fig. 1). Recently, various approaches have emerged to model the structural behaviors of origami which may be grouped into three categories that vary in complexity and generality: (1) Analytical solutions for elasticity problems related to origami have been developed where typically a unit cell or a portion of the pattern is explored empirically, e.g. Hanna et al. (2014), Qiu et al. (2016) and Brunck et al. (2016). These analytical approaches are typically suited for one specific origami pattern and cannot be readily used for other origami systems; they also often assume that deformation only occurs as folding along the prescribed fold lines. (2) A bar and hinge method where panel in-plane deformations are restrained using bars elements while bending of panels and folds is modeled using rotational hinges, e.g. Schenk and Guest (2011) and Wei et al. (2013). (3) Numerical

[☆] Dedicated to the memory of William "Bill" McGuire (1920–2013).

* Corresponding author.

E-mail address: paulino@gatech.edu (G.H. Paulino).

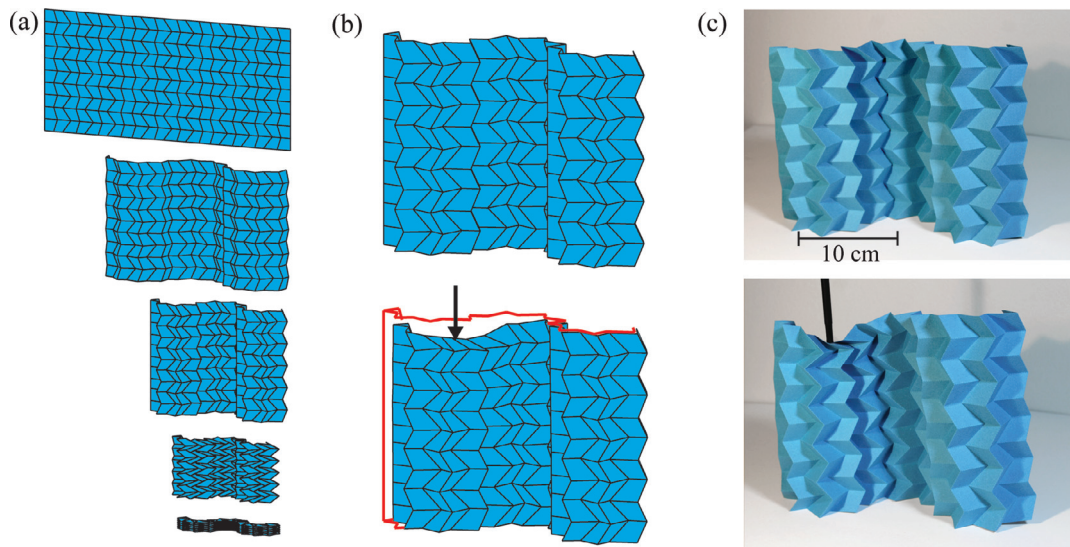


Fig. 1. A Miura-ori pattern with a modified curved geometry (Gattas et al., 2013). (a) Folding kinematics of the origami. (b) and (c) Initial (top) and deformed (bottom) shapes of the origami from a point load applied at the top, while the bottom of the structure is restrained vertically. (b) structural simulation with the bar and hinge model and (c) physical model of the origami.

methods, and particularly, finite element (FE) methods where the system is discretized in a detailed fashion, e.g. Schenk et al. (2014), Lv et al. (2014), Gattas and You (2015) and Peraza-Hernandez et al. (2016). The FE approach often provides higher accuracy, however, it tends to be computationally expensive, may obscure insight into the deformations, and depending on the discretization technique may not be suitable for studying patterns with different geometries.

This work aims to provide a method that is generally applicable to different folding patterns with a sufficient accuracy to capture important elastic behaviors. The model should be relatively computationally efficient to enable a full investigation of different families of origami shapes, and to allow optimization with variable parameters. We develop and explore a variation of the bar and hinge model that provides for scalable modeling of origami. To illustrate the practicality of the model, a real origami deformed by a physical load and a corresponding bar and hinge simulation are presented in Fig. 1. This paper also presents the stiffness characteristics of origami so as to effectively inform the bar and hinge model. In particular, three fundamental physical behaviors are explored: (1) stretching and shearing of thin sheet panels, (2) bending of the initially flat panels, and (3) bending along prescribed fold lines. The fundamental elastic behaviors are presented in Fig. 2 with a basic representation of how bars and hinges are used in a modeling framework. We provide scalable parameters that can be used for bar and hinge models to capture realistic behaviors of origami. This paper is motivated by the pioneering work of Prof. William “Bill” McGuire on matrix structural analysis (McGuire et al., 2000; Nilson et al., 2013).

The objectives of this paper are to (i) introduce and formulate the bar and hinge model, (ii) discuss the fundamental behaviors of thin sheets and provide a scalable implementation for how the model can capture these, and (iii) demonstrate techniques of how the model can be used for physical simulation. The paper is organized as follows: Section 2 discusses existing approaches for modeling origami and introduces the bar and hinge formulation used in this paper. The in-plane behavior of origami is explored in Section 3, out-of-plane bending of initially flat panels is studied in Section 4, and the bending along fold lines is discussed in Section 5. In Section 6, we discuss analysis for large displacements in origami, and in Section 7, we show examples of how

the model can be used for different studies of origami structures. Section 8 discusses the properties and limitations of the bar and hinge approach, and Section 9 provides concluding remarks.

2. Bar and hinge models for structural modeling of origami

In this paper, the bar and hinge approach is used to model origami with elastic behavior; such behavior is a combined result of in-plane deformation of panels, the bending of panels, and the folding along fold lines. We can observe that the geometry of folded paper with straight lines has a naturally discretized form that influences the elastic behaviors. First of all, because of the relatively high in-plane stiffness of the sheets, a straight fold line between surfaces tends to remain straight after adjacent material deforms. A panel surrounded by such creases is highly resistant to buckling, and as a result, a triangular face tends to remain planar, while a quadrilateral face tends to exhibit bending only along one of the diagonals (Fig. 2 middle column). The key idea of the bar and hinge model, is to follow this natural discretization as well as to provide scalable stiffness with the minimum number of elements. In these models the in-plane stiffness, both along fold lines and across the panel diagonals, is represented by bar elements with axial stiffness. The folding and bending stiffness is represented by elastic torsional hinges around the bars; see Fig. 2. From this simplification, our model ignores the local effect around the boundary edges (e.g. potential buckling), and thus in the current form, it would be difficult to deal with kirigami models where cuts on surfaces produce higher compliance.

The bar and hinge model can be used to analyze both flat foldable and non-flat foldable origami. The model is also suitable for both developable (origami that can be folded and developed starting from a flat sheet) and non-developable origami. The bar and hinge approach can be used in the study of surfaces not homeomorphic to a disk, such as origami tubes and cellular systems where multiple origami are stacked and assembled together. The model may also be used for the analysis of non-folding origami-like structures made of thin sheets (e.g. boxes and cartons). This paper only explores the model for rigid foldable systems; however, this is not a limitation of the model, but merely because of our interest in these structures, as they allow for continuous folding, simple actuation, and easy manufacturing. The bar and hinge

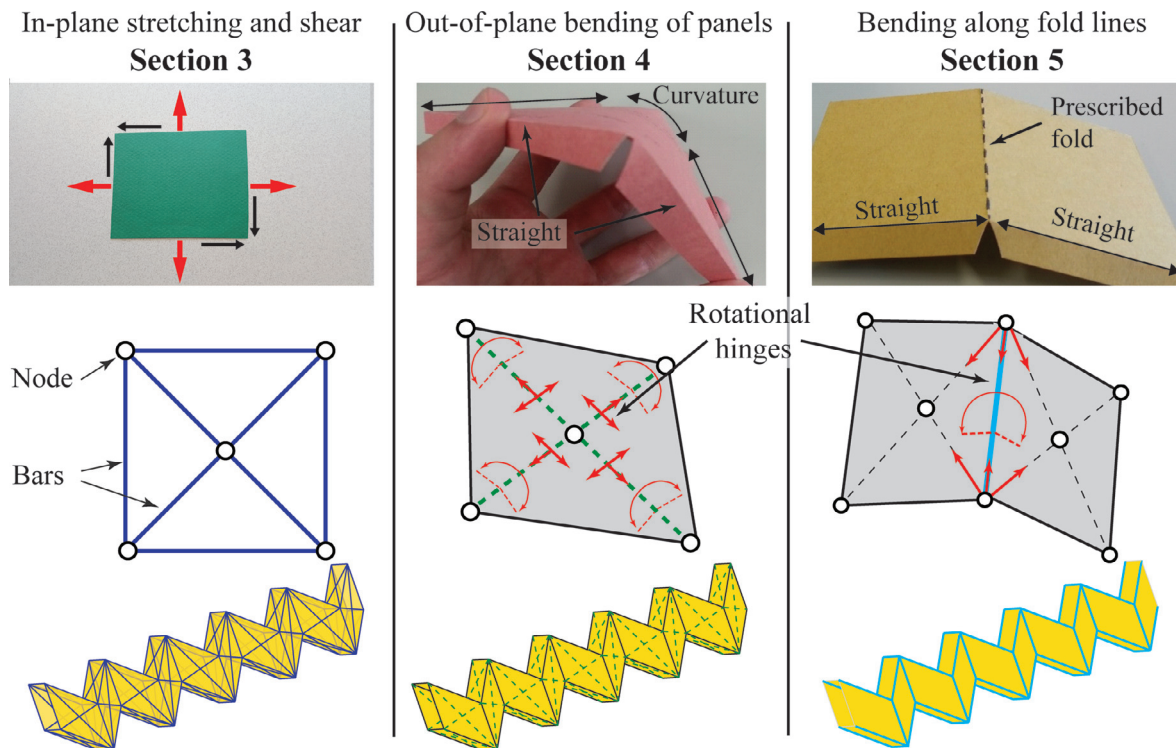


Fig. 2. The fundamental elastic behaviors of origami are discussed in this work. A physical paper model (top row), the bar and hinge placement for one panel in the model (middle row), and bar and hinge placement on an origami tube (bottom row). Bending of panels results in localized curvature about the shorter diagonal, while the fold lines are assumed to be more flexible and bend along a prescribed line. The behavior of each origami panel and fold (simulated using bars and hinges) can be placed into a global system model.

model can potentially be applicable to non-rigid foldable origami that exhibit multi-stability or nonlinear global buckling behaviors (Silverberg et al., 2015; Hanna et al., 2014; Waitukaitis et al., 2015).

The geometric versatility, simplicity, and efficiency are the main benefits of the bar and hinge model. The approach is suitable for a wide range of origami variations (e.g. Tachi (2009b); Gattas et al. (2013); Dudte et al. (2016)) and it is possible to parameterize the models to explore the influence of geometry on the structural properties. Bar and hinge models can explore foldability of a pattern in mechanical and physical terms (Saito et al., 2015; Fuchi et al., 2015; 2016b), in lieu of more mathematical derivations (e.g. Huffman (1976); Belcastro and Hull (2002); Hull (2012); Tachi and Hull (2016)). The simplicity of the model is valuable in understanding the behavior of origami and adjusting the model for different analyses. Eigenvalue simulations can be used to explore global folding and stiffness characteristics, and structural analyses can characterize the properties of origami inspired metamaterials that have unique and tunable properties (Tachi and Miura, 2012; Schenk and Guest, 2013; Silverberg et al., 2014; Lv et al., 2014; Cheung et al., 2014; Filipov et al., 2015; Yang and Silverberg, 2015). Over the last several years bar and hinge models have been used for various studies, and the model has evolved to provide more functionality and improved quality of analyses.

2.1. Evolution of bar and hinge models

Several bar and hinge models have been proposed, which vary in formulation and implementation. One of the earliest implementations is that by Schenk and Guest (2011) where four bars are placed on the perimeter of the panel and one bar is placed along the shorter diagonal of the panel. The model has four nodes and five bars, thus we designate this base of model as N4B5 (Fig. 3). It has become popular to use the bar

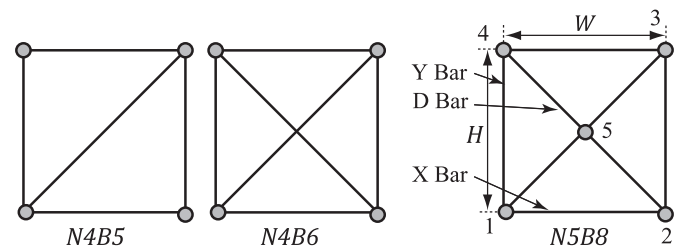


Fig. 3. Evolution of the bar and hinge models, where different orientations of bars and nodes are used to simulate the in-plane behavior of origami panels. The frame of bar elements can be used as one element to model the in-plane behavior for an entire origami panel. The added complexity from the N4B6 and N5B8 models makes it possible to include scalability, isotropy, accuracy and more functionality to the model. The N4B5 model is from Schenk and Guest (2011), the N4B6 is from Filipov et al. (2016), and the N5B8 is introduced in this work.

and hinge model with an energy approach to find the deformed shape of the structure (Bridson et al., 2003; Wei et al., 2013; Narain et al., 2013). The energy approach has been modified and has been used to provide fundamental studies on origami (Silverberg et al., 2014; Dudte et al., 2016). The N4B5 model has also been formulated based on elasticity and kinematics of solid state lattice systems (Evans et al., 2015). Another approach by Fuchi et al. (2016) uses frame elements instead of bars, and includes rotational degrees of freedom to enhance the flexibility of the model at the fold lines. This model can potentially capture more local bending and torsion behaviors in the origami, but the formulation becomes more complex. All N4B5 models cannot capture in-plane deformations isotropically, and thus they cannot incorporate accurate bar stiffness parameters. Inspired to overcome some of the limitations of the conventional N4B5 bar and hinge models, Filipov et al. (2016) presented a N4B6 model that

introduced an extra bar, making the frame indeterminate for in-plane loading (Fig. 3). By defining the bar properties, the model incorporates scaling effects and material properties. The indeterminate frame provides symmetric and isotropic response for in-plane loading. The model uses elastic modulus (E), Poisson's Ratio (ν), and thickness of the origami (t) along with length parameters to obtain scalable system behavior. One limitation of the N4B6 model is that, because of the crossed bars, large panel bending (large displacements) cannot be easily accommodated. Here, a modified approach is introduced where a node is incorporated at the connection of the panel diagonals. This model has five nodes and eight bars (N5B8), and is able to combine the benefits of both the N4B5 and N4B6. Some approaches for modeling of origami and thin sheets have also been formulated to account for in-plane stiffness using triangular finite elements (Resch and Christiansen, 1970; Phaal and Calladine, 1992b). If used to model quadrilateral origami, these approaches would lead to non-isotropic behavior for stretching and shear (see comparison in Section 3).

2.2. Model formulation for the bar and hinge approach

This section introduces the general formulation of a bar and hinge approach for modeling thin sheets in origami. The previously established model by Schenk and Guest (2011) is improved and extended. The global stiffness matrix for the origami sheet is constructed as follows:

$$\mathbf{K} = \begin{bmatrix} \mathbf{C} \\ \mathbf{J}_B \\ \mathbf{J}_F \end{bmatrix}^T \begin{bmatrix} \mathbf{D}_S & \mathbf{0} & \mathbf{0} \\ \mathbf{0} & \mathbf{D}_B & \mathbf{0} \\ \mathbf{0} & \mathbf{0} & \mathbf{D}_F \end{bmatrix} \begin{bmatrix} \mathbf{C} \\ \mathbf{J}_B \\ \mathbf{J}_F \end{bmatrix}, \quad (1)$$

The stiffness matrix (\mathbf{K}) for the origami structure incorporates stiffness parameters for panel *stretching* and *shearing* (\mathbf{D}_S), panel *bending* (\mathbf{D}_B), and *folding* along prescribed fold lines (\mathbf{D}_F). The compatibility matrix (\mathbf{C}) and Jacobian matrices (\mathbf{J}_B and \mathbf{J}_F) relate the stiffness of constituent elements (bars and hinges) to the nodal displacements, as discussed in detail in Sections 3.1 and 4.1. Each node has three displacement degrees of freedom (DOFs) and the stiffness matrix is thus of size $3n \times 3n$, with n being the total number of nodes in the system.

The total stiffness matrix is expressed equivalently as:

$$\mathbf{K} = \mathbf{C}^T \mathbf{D}_S \mathbf{C} + \mathbf{J}_B^T \mathbf{D}_B \mathbf{J}_B + \mathbf{J}_F^T \mathbf{D}_F \mathbf{J}_F = \mathbf{K}_S + \mathbf{K}_B + \mathbf{K}_F, \quad (2)$$

which makes it apparent that the total stiffness matrix of the origami structure has additive contributions from the bars (\mathbf{K}_S), the bending hinges (\mathbf{K}_B), and the folding hinges (\mathbf{K}_F).

In the following sections we incorporate scaling effects for the structure and make the panel stiffness dependent on material and geometric properties. The formulation for fold modeling is also updated, and a length scale parameter is used to define the bending stiffness of a fold. The model provides an improved basis for origami stiffness simulation, while keeping the formulation simple and modeling the origami components (panels and folds) as individual elements.

3. In-plane stretching and shear of flat thin panels

This section explores the behavior and stiffness of flat thin panels when subjected to in-plane loads (see left column of Fig. 2). The stiffness of stretching and shearing a thin sheet is typically several orders of magnitude greater than its bending stiffness as discussed in subsequent sections. Although bending and folding deformations will dominate in origami structures, it is important to capture the in-plane stiffness of panels.

Here, we study a single origami panel with different geometries subjected to in-plane loads. When assembled into a full origami system, multiple panels would interact and combine their in-plane

responses as determined by the global geometry of the system. The bar frame is used as a single element to model the in-plane behavior of the panel, thus at the connection of two panels, there will be two bars at the same location and connecting to the same two nodes. In this work, we assume that the material properties are locally isotropic and that the sheet behaves in the same way in all directions. The formulation is also based on an unbent panel; when a panel is bent out-of-plane, some of the stretching and shearing behaviors may change, but we feel that the bar and hinge model would provide a reasonable estimate of the stiffness and deformation. We also assume that the panel does not buckle, and that the bars remain straight and in-plane. This is a reasonable assumption because most panels are surrounded by creases with orthogonal panels, which act as stiffeners to prohibit panel buckling due to compression.

3.1. Definition of bar stiffness for the N5B8 model

Each of the bars in the indeterminate frame (N5B8 frame in Fig. 3) are defined to result in an isotropic and scalable behavior of the entire panel. A general formulation for bar elements is used where an equilibrium matrix (\mathbf{A}) relates internal bar forces (\mathbf{t}) to nodal forces (\mathbf{f}); a compatibility matrix (\mathbf{C}) relates bar nodal displacements (\mathbf{u}) to bar extensions (\mathbf{e}); and a diagonal matrix (\mathbf{D}_S) relates the bar extensions to the bar forces. The formulation can be written in three linear equations as

$$\mathbf{A}\mathbf{t} = \mathbf{f}, \quad \mathbf{C}\mathbf{u} = \mathbf{e}, \quad \mathbf{D}_S \mathbf{e} = \mathbf{t}. \quad (3)$$

Using the static-kinematic duality that $\mathbf{C} = \mathbf{A}^T$, the linear system for stretching and shear of the panels can be rewritten and is represented in Eq. (2).

The bar stiffness parameters (i.e. components of \mathbf{D}_S) are defined for each bar as

$$K_S = EA_e/L_e, \quad (4)$$

where L_e is the bar length and A_e is the bar area. When the indeterminate N5B8 frame is rectangular, the bar areas can be defined such that the frame will exactly exhibit Poisson effects for tensile loading in both directions (i.e. isotropic behavior). The bar areas are defined as:

$$A_X = t \frac{H^2 - \nu W^2}{2H(1 - \nu^2)}, \quad A_Y = t \frac{W^2 - \nu H^2}{2W(1 - \nu^2)}, \quad (5)$$

$$A_D = t \frac{\nu(H^2 + W^2)^{3/2}}{2HW(1 - \nu^2)},$$

for the horizontal (X), vertical (Y), and diagonal (D) bars, respectively. The isotropic behavior for a tensile load on a square panel is shown in Fig. 4(a). For tensile loads, a rectangular N5B8 frame will have a stiffness equivalent to a solid block of material (i.e. $EA/L = EWt/H$). These definitions are based on rectangular panels, however, in subsequent sections we show that these assumptions provide reasonable estimates when the panels are skewed.

When subjected to shear (Fig. 5) the frame stiffness is dependent on the chosen Poisson's ratio. From Eq. (5), when a low ν is used, the diagonal bars have a low area, and the frame demonstrates a low shear stiffness. The converse is also true, and increasing ν increases the shear stiffness. This behavior is opposite to real isotropic materials where shear stiffness decreases as ν increases. A serendipitous case occurs when ν is set to 1/3, and the behavior of the frame model in shear is identical to that of a homogeneous, isotropic block of material. As shown on the right of Fig. 5(d) the top of the frame displaces laterally in the direction of loading and each diagonal bar carries a force of $F/2$ in the X direction. The frame displacement matches the lateral displacement of a solid block with dimensions $W \times H \times t$ loaded in simple shear, analytically defined as $\Delta_x = F_X H / GWt$, where F_X is the total shear force

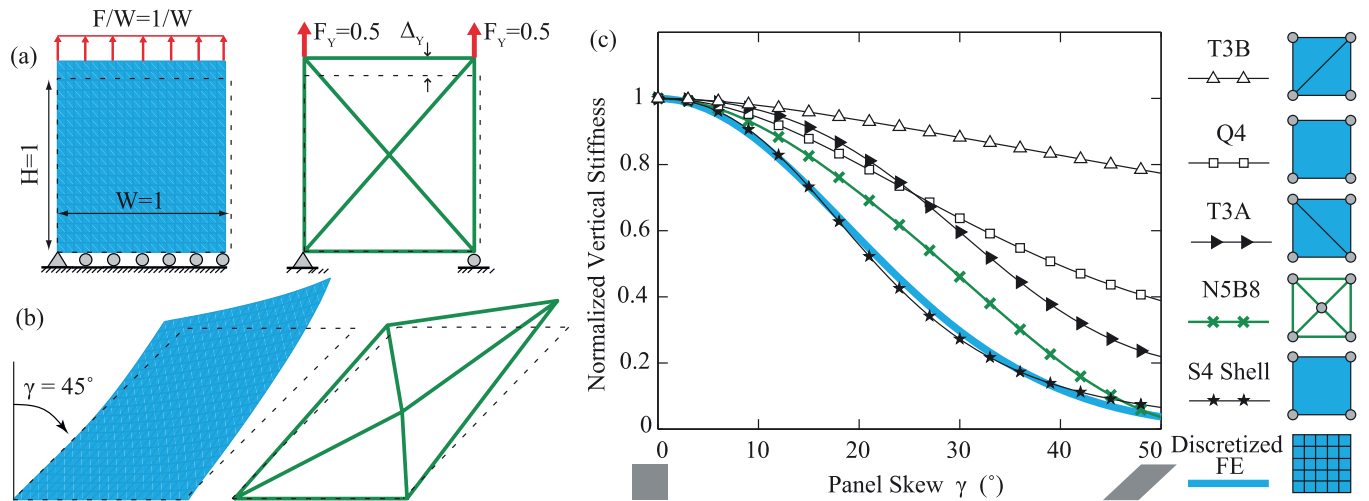


Fig. 4. Tensile test performed by applying a uniform distributed load to the top edge of a panel ($F = 1$) and restraining the bottom edge with a pin and rollers. (a) Deformed shapes of a square panel simulated with a discretized FE model (left) and the N5B8 model (right). Deformation is scaled by 1000 and undeformed outline is shown with dotted line. (b) Deformed shapes of skewed panels scaled by 100. (c) Normalized vertical stiffness of the panel with respect to the skew γ . The analysis is presented for the discretized FE case, the N5B8 model, and different FE cases using one or two elements only (S4 shell, Q4, T3A, and T3B).

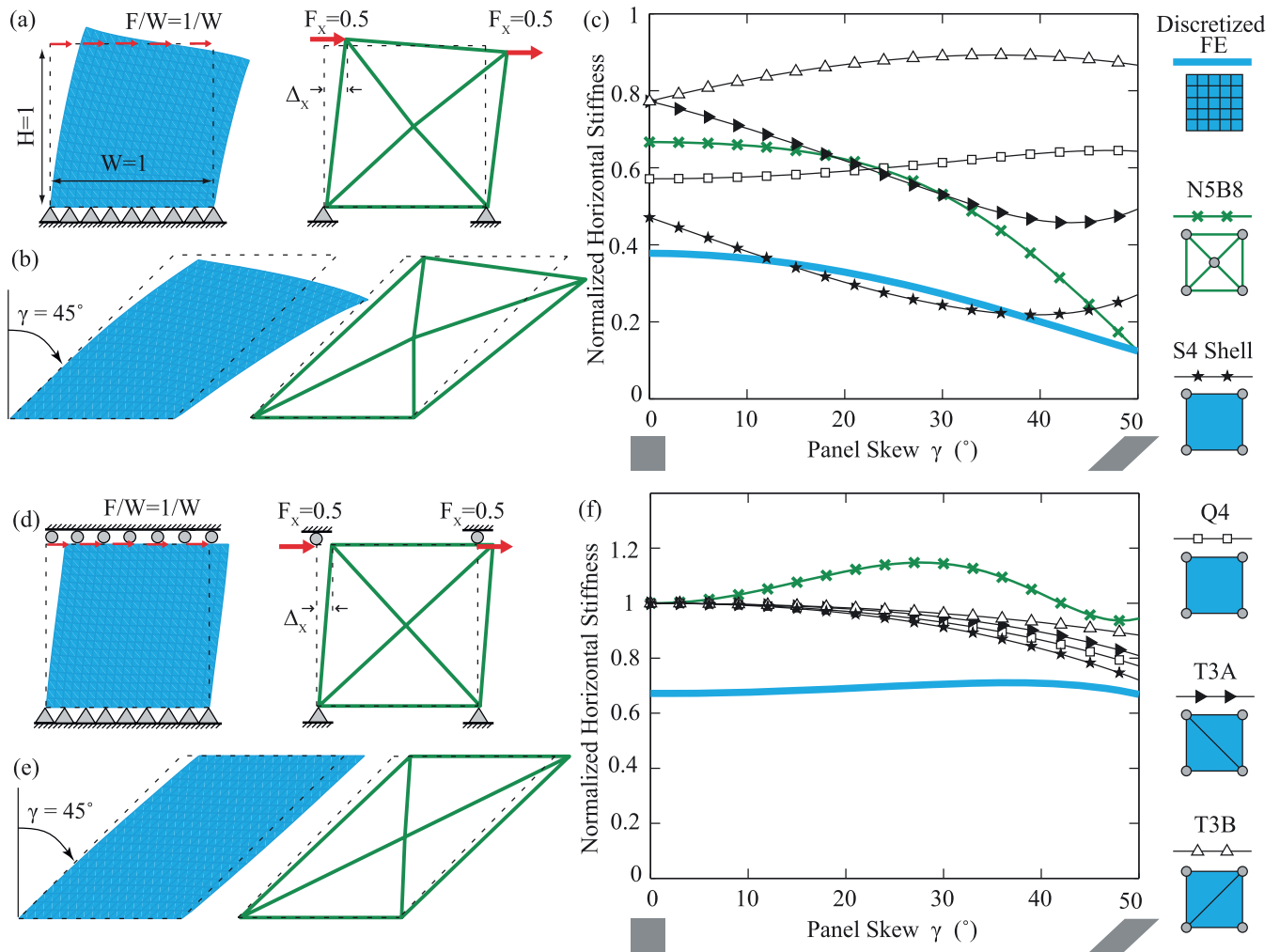


Fig. 5. Shear test performed by applying a uniform distributed load to the top edge of a panel ($F = 1$). In (a–c) only the bottom edge is restrained with pins, while in (d–f) the top edge is also restrained with rollers. (a) Deformed shapes of a square panel simulated with a discretized FE model (left) and the N5B8 model (right). Deformation is scaled by 300 and undeformed outline is shown with dotted line. (b) Deformed shapes of skewed panels scaled by 100. (c) and (f) Normalized horizontal stiffness of the sheet with respect to the skew γ . (d) and (e) Deformed shapes scaled by 300. The analysis is presented for the discretized FE case, the N5B8 model, and different FE cases using one or two elements only (S4 shell, Q4, T3A, and T3B).

and G is the shear modulus, defined as $G = E/2(1 + \nu)$ for a homogeneous, isotropic, linear elastic material. With $\nu = 1/3$, the frame is scale independent for shear loadings, similar to any generic FE approach.

When considering skewed and irregular panels, the height (H) of the panel is calculated as the average distance between nodes 1 to 4 and 2 to 3, while the width (W) is the average distance between nodes 1 to 2 and 4 to 3 (see Fig. 3). As will be shown in the subsequent section, these basic definitions provide a realistic behavior for the panel for various in-plane loads. In the future, it may be possible to find more advanced definitions for the individual bar stiffness that may improve the performance of the indeterminate N5B8 frame.

3.2. The stretching and shear of skewed panels

Fig. 4 portrays a flat thin panel subjected to a tensile test, where a uniform load of $F = 1$ is applied upward at the top of the panel, while the bottom is restrained in the vertical direction. The system is fully restrained out-of-plane. Using arbitrary units, the panel has a height and width of 1, a thickness of 0.01, and a Young's modulus of $E = 10^6$. A Poisson's ratio of $\nu = 1/3$ is used such that the N5B8 model exhibits a simple shear behavior.

As a reference, a discretized FE model is used to study the behavior of a flat thin panel. In this and subsequent sections of the paper the ABAQUS FE software (Abaqus, 2010) is used with the S4 general purpose shell elements with finite membrane strains that are appropriate for small and large deformation analyses. Mesh convergence studies for the stretching and shear examples showed that a discretization of 20×20 elements provide a displacement solution for a skewed panel that is within 0.013% of a mesh with double the number of DOFs.

The displaced shapes of the discretized FE and the N5B8 models are shown for square and skewed cases in Fig. 4(a) and (b) respectively. The N5B8 model is able to capture the isotropy of the panel and the general deformed shape relatively well. Fig. 4(c) shows the normalized vertical stiffness with respect to skew, where the behavior of the discretized FE model is considered an accurate representation of the real behavior. The vertical stiffness for each case is calculated as $K = F/(\Delta_Y)$, where Δ_Y is the average vertical displacement at the top surface of the panel. The stiffness is then normalized by the axial stiffness of the square piece of thin elastic sheet shown in Fig. 4(a) (i.e. by EWt/H). The different models used with number of DOFs active in-plane are: discretized FE - 1323 DOFs; N5B8 - 10 DOFs; a single shell (S4) - 12 DOFs; a quad (Q4) - 8 DOFs; and two triangular elements (T3A and T3B) - 8 DOFs. The S4 shells differ conceptually from the other elements in that they include drilling degrees of freedom at the four nodes. Fig. 4 shows that N5B8 model approximates axial stretching stiffness well for various amounts of skew. The model does not experience asymmetric stiffness which occurs due to the placement of the T3 elements.

Similar analysis are performed for two cases of shear applied to the thin panel. In one case, the element is restrained only on the bottom (Fig. 5(a)–(c)), and in the other it is restrained on both the top and bottom, and is subjected to (theoretically) simple shear (Fig. 5(d)–(f)). The shear stiffness is calculated as $K = F/(\Delta_X)$, where Δ_X is the average horizontal displacement at the top surface of the panel. The stiffness is then normalized by the shear stiffness of a square piece of thin elastic sheet subjected to simple shear (i.e. by GtW/H). The N5B8 and other single element models typically overestimate the shear stiffness by about 30–80%. Of particular interest is the simple shear case with no skew ($\gamma = 0^\circ$) where most models match the stiffness of a simple shear panel, while in reality the discretized case is more flexible. The higher

flexibility occurs because the material in an actual panel experiences both tension and shear, and not theoretical simple shear.

Although the N5B8 model overestimates the shear stiffness for both cases, it follows similar trends to the discretized FE analysis. When not restrained on top, the shear stiffness reduces with skew, and when restrained on top the shear stiffness slightly increases and then decreases with higher skew. The deformed shape for shear loading of the N5B8 model is similar to the discretized FE case, but the displacements are underestimated. It should be noted that linear elastic shear in a complete origami structure would likely be more complex than the two cases presented here, as it may be accompanied with moments and localized axial forces. In summary, the N5B8 model is capable of capturing tensile isotropic deformations of flat thin panels with and without skew. The model approximates axial stiffness well, and although it overestimates shear stiffness, the stiffness follows expected trends with respect to skew.

4. Out-of-plane bending of flat panels

The out-of-plane bending of origami panels presents an interesting phenomenon because adjacent panels can restrict bending (see middle column of Fig. 2). This restriction prevents the panel from bending with a single curvature over the length of the long axis, and instead a more complicated bending occurs where the panel deforms along its diagonals (Demaine et al., 2011). This phenomenon tends to be more pronounced for large deformation bending and has been studied in previous research (Lobkovsky et al., 1995; Di Donna and Witten, 2001; Witten, 2007). For modeling of origami, we investigate the stiffness of both small and large deformation bending of the thin panels. The bar and hinge models use an angular constraint to approximate the deformation and stiffness of panel bending. By studying the detailed bending of thin panels we formulate empirical expressions for the bar and hinge model that scale stiffness based on material and geometric effects.

4.1. Rotational hinges for out-of-plane bending

Early implementations of the bar and hinge model use two triangular segments connected by an angular constraint along one diagonal to model the global out-of-plane displacement of the panel (Fig. 6(a)). The choice of the diagonal does not influence the displacement pattern for small displacements (Schenk and Guest, 2013), but typically the shorter diagonal (with triangular segments 1-2-3 and 1-3-4) is used to better match the expected real world behavior. For the N5B8 model, we have one additional out-of-plane degree of freedom at node 5. The panel is divided into four triangular segments with bending possible about both diagonals. The equivalent compatibility matrix for the hinges (including bending and folding) contains the linearized constraint functions that restrict the relative rotations between adjacent triangular segments (Fig. 6(b)). By assigning a finite angular stiffness, which is stored in the diagonal matrix \mathbf{D}_B , to each relative rotation between triangular segments, a variation from the initial flat state results in (internal) resistance forces. Each angular constraint is formulated separately based on the dihedral angle(s), θ_i , which can be calculated by using cross and inner products of the vectors \mathbf{a} , \mathbf{b} , \mathbf{c} and \mathbf{d} from the nodal coordinates of the panel \mathbf{p} . Linearization of the angular constraint yields the Jacobian for panel bending, \mathbf{J}_B , which is calculated as

$$d\theta_i = \sum \frac{\partial \theta_i}{\partial p_j} dp_j = \mathbf{J}_B \mathbf{u}, \quad (6)$$

where \mathbf{u} are the displacements of the nodes. The Jacobian is the equivalent compatibility matrix for the bending hinges, as matrix

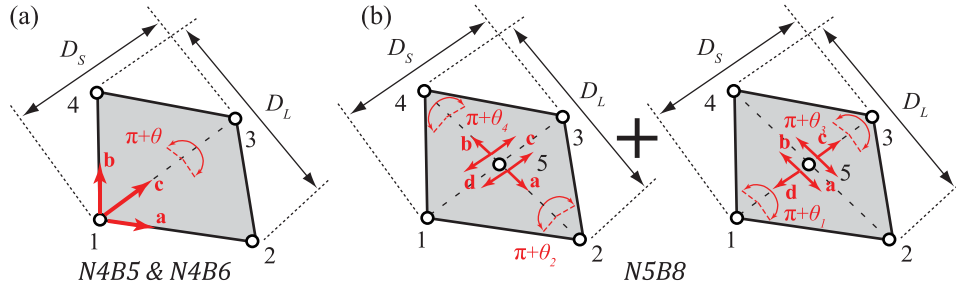


Fig. 6. Placement of rotational hinges in the different bar and hinge models. The hinges provide stiffness for out-of-plane deformations of the panels.

\mathbf{C} is for bars. Eq. (2) incorporates panel bending stiffness where each element in the diagonal matrix \mathbf{D}_B corresponds to the bending stiffness for an angular constraint. Considerations for defining the bending stiffness of each constraint K_B are discussed in the following section.

The bending definition here is similar to that used by other researchers (Schenk and Guest, 2011; Phaal and Calladine, 1992). Although the N5B8 model allows for bending along either diagonal, in Section 4.2 we discuss that this poses a problem for accurately capturing the stiffness. We make a modification to restrict bending about the long diagonal by making those rotational hinges approximately 100 times stiffer. This modification is not necessary for large displacement results. However, it allows for an accurate representation of panel bending stiffness, and thus is used for both small and large displacement cases. The deformed shapes with this modification consist of bending about the short diagonal only, and thus the N5B8 model is effectively reduced to a N4B5 model for panel bending.

4.2. Panel bending stiffness: from small to large displacements

This section presents the stiffness characteristics of thin restrained panels and introduces the stiffness definitions for bending in the N5B8 model. Appendix A provides additional information on the specific stiffness scaling properties used herein. The origami panels are restrained, meaning that there are adjacent panels positioned out-of-plane along the edges (at fold lines), and thus these orthogonal panels limit out-of-plane deformation of the flat sheet. Fig. 7(a) and (b) shows a FE discretization of a restrained rhombus panel with a long diagonal $D_L = 1.4$, a short diagonal $D_S = 1.0$, and four restraining panels with a vertical width of 0.4. Boundary conditions are imposed on three corners and a displacement control is placed on the fourth. We constrain the minimum six degrees of freedom to make the system statically determinate. With the problem set-up, it is possible to achieve panel bending along either of the two diagonals of the restrained panel. For different geometries of this problem, we have verified that for large displacements, bending always occurs about the shorter diagonal and thus we limit the dimensions to $D_S < D_L$. For subsequent analyses, we apply a displacement control trajectory that follows a rotation of the bending angle θ_B about the short diagonal. The vertical reaction on the left corner (R_A) is used to calculate the bending moment about the sheet as $M_B = R_A D_L / 2$.

The problem converges successfully, and our chosen discretization of 30×30 shell elements for the flat sheet provides solutions that are close to a FE model with double the number of DOFs (0.12% difference for small deformations $\theta_B = 0.1^\circ$ and 0.21% for large deformations $\theta_B = 70^\circ$). The moment bending relation of the entire panel can be represented as $M_B = \theta_B K_B$, which can subsequently be used to formulate the stiffness for the angular constraints. The FE analysis from small to large displacements for three sheets with different geometries is shown in Fig. 7(e).

The in-plane stiffness of the thin adjacent panels is high enough to prevent bending and buckling at the edge connecting two panels (i.e. at the fold line on the perimeter of a panel). Because of this restriction, the stiffness is higher than that of unrestrained sheets that are free to bend along the edges. The bending stiffness of the restrained sheet scales with $k(D_S/t)^{1/3}$ where k is the bending modulus of the sheet, defined as $k = Et^3/12(1 - \nu^2)$ (Lobkovsky et al. (1995) and Appendix A).

The small displacement behavior for restrained origami panels had not been explored in detail previously. When a relatively small bending angle ($\theta_B \lesssim 6^\circ \approx 0.1\text{rad}$) is imposed, the panel experiences double curvature with bending along both diagonals (Fig. 7(a)). The double curvature matches expected behavior. The bending moment relation remains linear for small displacements: the moment scales with θ_B , and the energy scales with θ_B^2 . There is no tension in the sheet, and bending energy is distributed throughout the panel with higher concentration at the corners on the short diagonal (Fig. 7(a)). The bending stiffness for small deformation bending is highly dependent on the geometry of the panels which is explored in detail in Appendix A. The stiffness scales with a parameter $\Sigma\alpha$ that is introduced to describe the corner geometry of the short diagonal. The parameter $\Sigma\alpha = \alpha_1 + \alpha_2 + \alpha_3 + \alpha_4$ represents the deviation of the short diagonal corners from being flat edges where the restraining panels on the side are collinear (see results and cutout in Fig. 7(e)). A square panel will have all corners of 90° and $\Sigma\alpha = 180^\circ = \pi$. Based on the scaling observations the bending moment for small displacements of the panels can be formulated as

$$M_{BS} = \theta_B \left(0.55 - 0.42 \frac{\Sigma\alpha}{\pi} \right) \frac{Et^3}{12(1 - \nu^2)} \left(\frac{D_S}{t} \right)^{1/3}. \quad (7)$$

The equation is suitable for panel geometries in the range of $\pi/2 < \Sigma\alpha < \pi$, which would satisfy most origami structures.

For the large displacement analyses ($\theta_B \gtrsim 23^\circ \approx 0.4\text{rad}$), we observe the same global behaviors as Lobkovsky et al. (1995). The bending becomes restricted along the short diagonal D_S (Fig. 7(b)). In this case, tensile forces develop over the sheet's surface, and flexural deformations become restricted to a small area focused at the bending ridge. For large displacements, stiffness is not significantly affected by the panel geometry and boundary conditions, and the bending moment scales with $\theta_B^{4/3}$. This behavior differs from a linear hinge and, in contrast, the restrained panel becomes stiffer with larger bending angles (Fig. 7(e) and Appendix A). The bending moment for large displacements can be approximated as

$$M_{BL} = \theta_B^{4/3} (1.0) \frac{Et^3}{12(1 - \nu^2)} \left(\frac{D_S}{t} \right)^{1/3}. \quad (8)$$

Eqs. (7) and (8) are used to inform the stiffness parameters for the bar and hinge models. Each of the stiffness components in the diagonal matrix \mathbf{K}_B (see Eq. (2)) are defined using the small defor-

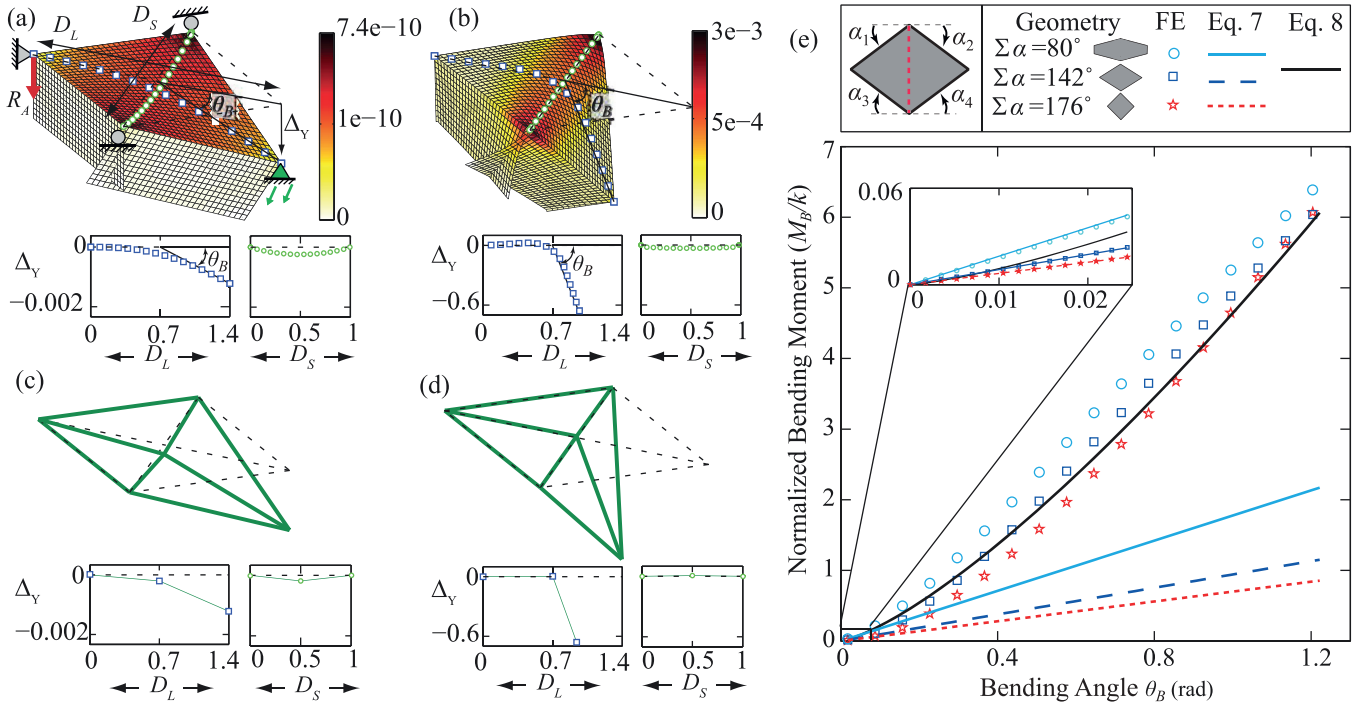


Fig. 7. Bending behavior of thin panels with restrained edges. (a) and (b) FE discretized thin sheet with restrained edges bent about the shorter diagonal. The total energy in each element is shown with color. (c) and (d) show the panel bending simulated with the bar and hinge model. In (a) and (c) the sheet is bent with $\theta_B = 0.1^\circ$, and displacements are scaled by 300. In (b) and (d) the sheets are bent with $\theta_B = 70^\circ$. In (a) through (d) displacements along the diagonals are shown below the deformed structure. (e) The bending moment normalized by k vs. bending angle for different geometries of thin restrained sheets. The numerical FE solutions (points) are plotted together with the bar and hinge solutions (lines) defined using Eqs. (7) and (8).

mation relations as

$$K_B = \left(0.55 - 0.42 \frac{\Sigma\alpha}{\pi} \right) \frac{Et^3}{12(1-\nu^2)} \left(\frac{D_S}{t} \right)^{1/3}. \quad (9)$$

The N5B8 model can be used to capture both small and large displacements. Because two rotational hinges are used on each diagonal of the panel, half of the appropriate stiffness ($K_B/2$) is placed on each rotational constraint. The deformed shape in Fig. 7(c) is obtained by using Eq. (9) to define each angular constraint with the corresponding diagonal (D_S or D_L). This allows for the central node to deform downward and the deformed shape looks similar to the FE results with bending along both diagonals. This approach also provides a good approximation for the displaced shape with large displacements because bending occurs primarily about the short diagonal, which is more flexible. Unfortunately, Eqs. (7)–(9) assume panel bending in only one direction, thus the stiffness of the N5B8 model is lower when both diagonals are defined with these approximations. A better stiffness approximation is obtained when the short diagonal is defined based on Eqs. (7)–(9), and the long diagonal is defined to be approximately 100 times stiffer. This adaptation provides a reasonable representation of panel bending stiffness and the deformed shapes consist of bending about the short diagonal. Future studies could be pursued to define both the short and long diagonals in a manner that would capture an accurate deformed shape and stiffness simultaneously.

5. Bending along prescribed fold lines

Fold lines (or hinges) between two origami panels, is where bending is intended to occur for the kinematic folding of origami (see right column of Fig. 2). The characterization, modeling, and behavior of the fold lines has been a wide topic of study, and there

is not a one single approach that can be used for all origami structures and systems. Appendix B contains a summary of crease type folds and provides a quantitative study on their stiffness in scalable terms. The behavior of composite and hinged origami would likely be dependent on the specific design, and scalable stiffness properties can be explored on an individual basis.

When performing detailed modeling of fold lines, it is possible to include a finite fold width (Peraza-Hernandez et al., 2016), or to account for an offset that accommodates hinges and the material thickness (Edmondson et al., 2014; Chen et al., 2015). However, for most origami, the fold width can be considered negligible, and the fold is assumed to lie on the center of the adjacent panels. We make these assumptions for our model, and we are able to simulate the bending moment behavior of the fold line by connecting adjacent panels with a rotational hinge. In this paper, we use a linear elastic bending moment behavior at the fold lines, however the model can be adapted to capture nonlinearity (e.g. Giampieri et al. (2011); Mentrastrì et al. (2013b)).

5.1. Rotational hinges for fold line bending

The folds are modeled in a similar fashion to the bending of panels. Realistic origami behavior does not allow for out-of-plane displacements along fold lines due to the restrictive nature of the sheets that form fold lines (Section 4). Thus, it is sufficient to use this simplified approach where the origami fold is modeled as a rotational hinge along a straight edge. A schematic of the fold model contains a fold spanning nodes 2 and 3 connecting two panels (1-2-3-4 and 2-5-6-3) (Fig. 8). In the N4B5 and N4B6 models, the angular constraint formulation (Section 4.1) is used for two independent fold elements from the two vector sets: (1) **a**, **b**, and **c** and (2) **-a**, **d**, and **e**. The N5B8 model can use an alternative set of rotational constraints that connect to the central (inside) node: (3) **a**, **f**, and **g** and (4) **-a**, **h**, and **i**. For this work, we use the con-

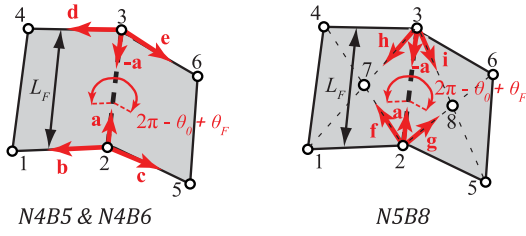


Fig. 8. Placement of rotational hinges to capture the fold line stiffness. The rotational constraints for the N5B8 model includes only the central nodes of the panel and thus removes the ambiguity between fold and panel bending for large displacement analyses.

straints of only the inside node because this removes ambiguity between panel and fold bending (e.g. in the N4B5 a node 5 motion out of plane signifies both panel and fold bending). In Section 5.2, we show that the inside node constraints provide a reasonable estimate of the deformed shape when both panel and fold bending is considered. The initial fold angle (θ_0) represents the origami at a static and unstressed state. This angle could be different for different folds on the origami, and can be calculated using basic geometric relations for each chosen configuration. Here, the angle θ_F represents a rotation away from the initial static configuration.

5.2. Scalable stiffness parameters for fold lines

We assume that the behavior over the length of the fold line is constant, and that the bending moment for the fold can be obtained from $M_\ell = \theta_F K_\ell$ where the factor K_ℓ represents the rotational stiffness of the fold line. The subscript ℓ indicates that this is the *local* folding behavior over the infinitesimal small width of the fold, and that the behavior of the adjacent panels is not included. Based on previous research (Lechenault et al., 2014; Pradier et al., 2016), it is expected for K_ℓ to scale with the length of the fold line (L_F) and the bending modulus of the thin sheet (k). Thus the localized stiffness of the fold line can be obtained as

$$K_\ell = \frac{L_F}{L^*} k = \frac{L_F}{L^*} \frac{Et^3}{12(1-\nu^2)}, \quad (10)$$

where a length scale factor L^* (in units of length) defines the relative stiffness of the fold based on the material, fabrication, and geometric properties. The length scale factor L^* is assumed to increase with the thickness of the sheet (Lechenault et al., 2014). However, there is currently no physical basis for determining the length scale, other than from experimental data (see Appendix B). Here, we follow the same methodology and use L^* , however, we acknowledge that future research may bring about alternative methods to quantify the local fold stiffness.

These scale independent definitions can be used for the fold stiffness in the bar and hinge model, as well as other simplified approaches. However, as currently presented, Eq. (10) can result in an unrealistically high fold stiffness as L^* approaches zero. An infinite stiffness may be realistic on a local scale (e.g. when there is no fold), however the global stiffness of the fold would be limited by the flexibility of adjacent panel material.

Fig. 9 demonstrates how the local fold stiffness and adjacent material behave for different L^* . We use 30 mm panels, with a thickness of 0.36 mm to allow a length to thickness ratio of ≈ 100 for the short panel diagonals. This thickness is also close to many of the experiments discussed in Appendix B. An FE model is used where the panels and adjacent panels are simulated with shell elements. The localized fold line is simulated using collocated nodes that are joined in the three Cartesian directions. A rotational spring is placed at each pair of collocated nodes to simulate the local stiffness of the fold line (i.e. Eq. (10)).

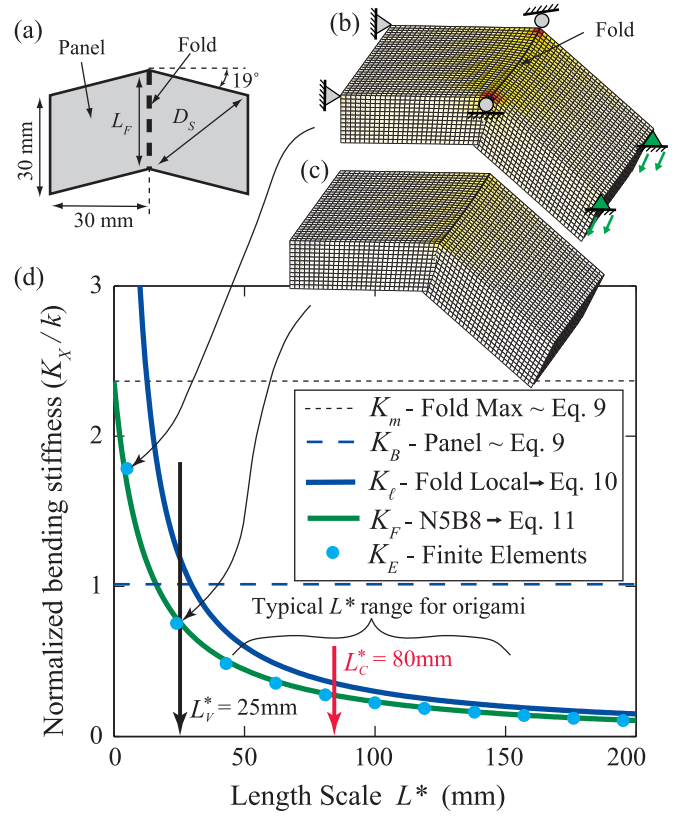


Fig. 9. Bending of a fold line that connects two restrained panels with $t = 0.36$ mm. Large displacement analyses are performed with $\theta_F = 40^\circ$. (a) Schematic of the fold and the two skewed panels with a geometry parameter of $\Sigma\alpha = 142^\circ$. (b) Bending of a FE model where the localized fold line is much stiffer than adjacent material ($L^* = 5$ mm). Double curvature bending occurs similar to a sheet with no fold line. (c) Bending of the system where the localized fold line is stiffer than most origami ($L^* = 25$ mm). Bending occurs primarily at fold line. (d) The normalized bending stiffness of the fold and the adjacent panels. The maximum and panel stiffness (K_m and K_B) are calculated with different variables (from Eq. (9)), while the local (K_ℓ) and combined (K_F) fold stiffness are plotted for different L^* values (from Eqs. (10) and (11) respectively). We show representative values of the length scale for the virgin (L_v^*) and the cyclic (L_c^*) tests.

The bending stiffness is calculated using a large displacement analysis, where the fold is bent to $\theta_F = 40^\circ$. The stiffness is normalized by k , and compared to different fold definitions and the adjacent panel (K_B calculated from Eq. (9)). In a case where an unrealistically high stiffness is used for the fold (Fig. 9(b)), the system deforms similar to the minimal ridge case (see Appendix A). Thus, we introduce a *maximum* fold stiffness K_m that represents the stiffness of adjacent panel material. We assume the case of a minimal ridge and calculate K_m with Eq. (9) where we substitute L_F for D_S and assume $\Sigma\alpha = 0$. For the example in Fig. 9 $K_m = 2.4k$. Considering that the localized fold and the adjacent material act in series, we calculate a combined fold stiffness as

$$K_F = 1 / (1/K_\ell + 1/K_m). \quad (11)$$

The introduction of K_m limits the maximum stiffness of the fold when L^* is low (Fig. 9(d)). The precise value of K_m is not important for the analysis, and the N5B8 model provides a reasonable estimate for fold stiffness when either half or double the value of K_m is used. Bending of the adjacent panels typically has a higher stiffness than the fold line ($K_B > K_F$) for the typical origami range (realistically large values of L^*). In extreme cases where a fold is intentionally restricted from folding ($L^* < L_v^*$), the entire fold assembly may be about two to three times stiffer than the adjacent panels. Thus, if the panel to fold stiffness ratio is used for evaluat-

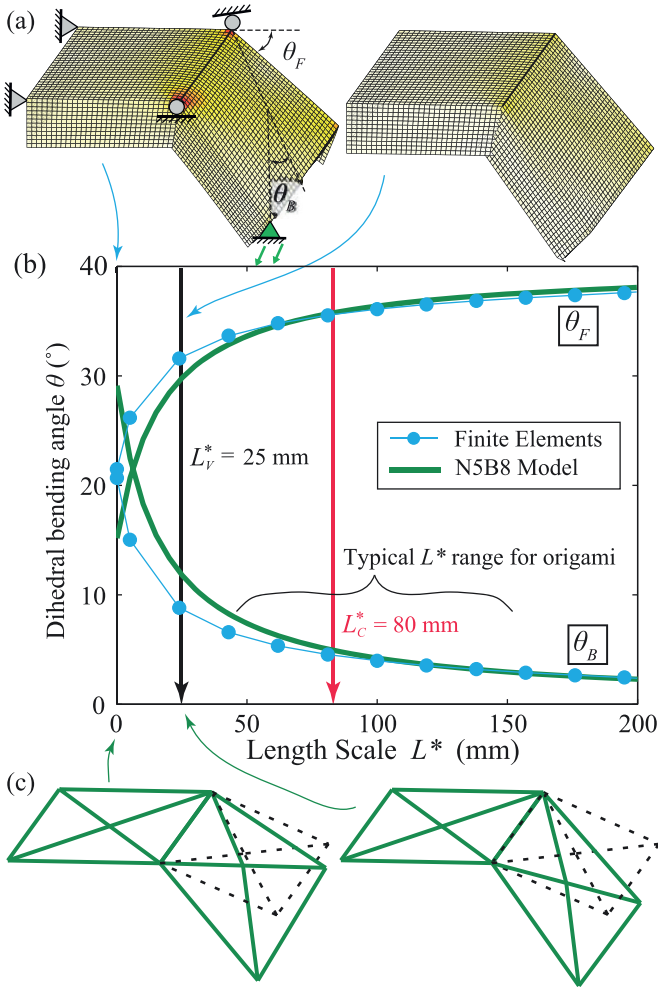


Fig. 10. Asymmetric bending of the fold system from Fig. 9. (a) Bending of a FE model with folds stiffer than typical origami ($L^* = 1$ mm left and $L^* = 25$ mm right). When the fold stiffness reaches realistic origami stiffness values ($L^* > 25$ mm) bending occurs primarily along the fold. (b) The folding angle of the fold (θ_F - top) and the adjacent panel (θ_B - bottom) with respect to the length scale parameter (L^*) for a FE model and the N5B8 model. (c) Fold and panel bending simulated with the N5B8 model.

ing system behavior, a range of $K_B/K_F = 1/3$ to 20 would provide a realistic estimate. The ratio may change slightly for different thickness of the material or L/t ratios.

Eq. (11) can be used to define the fold stiffness in different bar and hinge models, as well as other phenomenological models where fold lines are simplified to a rotational hinge (e.g. Qiu et al. (2016)). We use an FE model and the N5B8 model to explore the asymmetric bending of a fold and adjacent panel where only one side of the panel is displaced downward (Fig. 10). As shown in Fig. 8 the connectivity of the fold line in the N4B5, N4B6, and N5B8 models is performed using two rotational hinges. Half of the stiffness from Eq. (11) is distributed to each rotational constraint. The N5B8 model is able to capture the deformed state of the system for realistic values of L^* (Fig. 10).

6. Large-displacement analysis of origami

The bar and hinge model can be adapted to capture nonlinear and multi-stable behaviors associated with origami. Compared to linear analysis (see Section 2.2), the equilibrium function becomes a nonlinear function of the displacements. Assuming the applied

force is \mathbf{f} , denoting \mathbf{T} as the internal force vector, the equilibrium (governing equation) is written as:

$$\mathbf{T}(\mathbf{u}) = \mathbf{f}. \quad (12)$$

In (displacement-based) linear analysis, \mathbf{T} is a linear function of the displacement \mathbf{u} , and thus $\mathbf{T} = \mathbf{K}\mathbf{u}$, leading to the well-known expression of $\mathbf{K}\mathbf{u} = \mathbf{f}$. In large displacement analysis, the internal force vector becomes a nonlinear function of the displacements. As a consequence, the stiffness matrix is no longer a constant matrix, and must be updated at each displacement iteration.

The N5B8 has been implemented in the MERLIN software (Liu and Paulino, 2016). The formulation for large displacement analysis is summarized here and a complete derivation can be found in Liu and Paulino (2017). We show the change of the formulation from the linear elastic to a formulation that incorporates nonlinearity. To simplify the derivations presented here, the Saint Venant–Kirchhoff model is adopted as the constitutive equations for bar elements. However, other nonlinear constitutive models can also be adopted within the N5B8 framework. The presented nonlinear formulation is an extension of the linear elastic formulation. For the hinges that simulate bending of the panels, Eq. (8) as explained in Section 4 is used. For the hinges that simulate fold lines, we assume that the behavior remains linear even for large deformations, i.e., the stiffness K_F remains constant.

Similar to the linear case, the strain energy of the structure has contributions from the bars, bending hinges and folding hinges. The total potential energy of the system is then:

$$\Pi = U_S + U_B + U_F - V, \quad (13)$$

where V is the potential energy due to externally applied load \mathbf{f} . By applying the Principle of Stationary Potential Energy, the equations of equilibrium, and therefore the finite element matrices, can be derived. They take the following form:

$$\mathbf{T} = \mathbf{T}_S + \mathbf{T}_B + \mathbf{T}_F - \mathbf{f}, \quad (14)$$

$$\mathbf{K} = \mathbf{K}_S + \mathbf{K}_B + \mathbf{K}_F, \quad (15)$$

which is the same general form as in the linear elastic formulation.

6.1. Enriched formulation for bars

Denote ϵ_{xx} as the one-dimensional Green–Lagrange strain tensor (under uniaxial load). The one-dimensional 2nd Piola–Kirchhoff stress tensor becomes a linear function of the Green–Lagrange strain according to the Saint Venant–Kirchhoff model (Wriggers, 2008):

$$S_{xx} = E\epsilon_{xx}, \quad (16)$$

where E is the Young's modulus. The Green–Lagrange strain relates to the nodal displacements by (Wriggers 2008):

$$\epsilon_{xx} = \frac{1}{L_e} \mathbf{C}_e \mathbf{u}_e + \frac{1}{L_e^2} \mathbf{u}_e^T \mathbf{G} \mathbf{u}_e, \quad (17)$$

where \mathbf{u}_e is the local displacement vector associated with a bar element e , and \mathbf{C}_e contains the directional cosines of the bar, which, when expressed with the global indexing of degrees of freedom, is a row of the compatibility matrix \mathbf{C} as mentioned in Section 2. The matrix \mathbf{G} is defined as:

$$\mathbf{G} = \begin{bmatrix} \mathbf{I}_{3 \times 3} & -\mathbf{I}_{3 \times 3} \\ -\mathbf{I}_{3 \times 3} & \mathbf{I}_{3 \times 3} \end{bmatrix}. \quad (18)$$

Correspondingly, the associated elemental internal force vector and tangent stiffness matrix are expressed as:

$$\mathbf{T}_{S(e)} = S_{xx} A_e \left(\mathbf{C}_e^T + \frac{1}{L_e} \mathbf{G} \mathbf{u}_e \right), \quad (19)$$

$$\mathbf{K}_{S(e)} = \mathbf{K}_{S(e)}^{LE} + \mathbf{K}_{S(e)}^1 + \mathbf{K}_{S(e)}^2 + \mathbf{K}_{S(e)}^G. \quad (20)$$

The subscript $S(e)$ means that the term is an elemental component to the global internal force vector or stiffness matrix associated with the bars (i.e. \mathbf{T}_S and \mathbf{K}_S). The matrix $\mathbf{K}_{S(e)}^{LE}$ is the linear stiffness matrix, which is the elemental component of the stiffness matrix \mathbf{K}_S in Eq. (2), $\mathbf{K}_{S(e)}^G$ is the geometric stiffness matrix, and $(\mathbf{K}_{S(e)}^1 + \mathbf{K}_{S(e)}^2)$ forms the initial displacement matrix. The terms are elaborated as follows:

$$\mathbf{K}_{S(e)}^{LE} = (EA_e/L_e) \mathbf{C}_e^T \mathbf{C}_e, \quad (21)$$

$$\mathbf{K}_{S(e)}^1 = (EA_e/L_e^2) [(\mathbf{G} \mathbf{u}_e) \mathbf{C}_e + \mathbf{C}_e^T (\mathbf{G} \mathbf{u}_e)^T], \quad (22)$$

$$\mathbf{K}_{S(e)}^2 = (EA_e/L_e^3) [\mathbf{G} \mathbf{u}_e][\mathbf{G} \mathbf{u}_e]^T, \quad (23)$$

$$\mathbf{K}_{S(e)}^G = (S_{xx} A_e/L_e) \mathbf{G}. \quad (24)$$

6.2. Enriched formulation for bending and folding hinges

The internal force vector and tangent stiffness matrix of each bending hinge are also enriched with higher order terms to capture the nonlinear behavior. They are expressed as follows, for the i th bending hinge:

$$\mathbf{T}_{B(i)} = M_{BL} \frac{d\theta_i}{d\mathbf{p}}, \quad (25)$$

$$\mathbf{K}_{B(i)} = K_{BL} \frac{d\theta_i}{d\mathbf{p}} \otimes \frac{d\theta_i}{d\mathbf{p}} + M_{BL} \frac{d^2\theta_i}{d\mathbf{p}^2}, \quad (26)$$

where,

$$K_{BL} = \frac{\partial M_{BL}}{\partial \theta_i}. \quad (27)$$

Notice that,

$$K_{BL} \frac{d\theta_i}{d\mathbf{p}} \otimes \frac{d\theta_i}{d\mathbf{p}} = K_{BL} \mathbf{J}_{B(i)}^T \mathbf{J}_{B(i)}. \quad (28)$$

The term in Eq. (28) is the elemental component of \mathbf{K}_B in Eq. (2). The vector $\mathbf{J}_{B(i)}$ is a row of \mathbf{J}_B in Eq. (6), when assembled into global degrees of freedom. The second term in Eq. (26) is a higher order term which accounts for geometric nonlinearity associated with a rotational hinge. An identical procedure applies to the folding hinges.

To conduct a nonlinear analysis, a Newton–Raphson iterative procedure can be used to solve the nonlinear equilibrium equation. However, in many occasions, origami structures may deform with severe nonlinearity and multi-stability. Therefore, advanced nonlinear solvers (i.e. numerical continuation algorithm) such as the arc-length methods can be used to capture the full equilibrium path of an origami structure under certain loading. In our implementation, the Modified Generalized Displacement Control Method (Leon et al., 2014) is adopted, which yields an equivalent linearized cylindrical constraint equation. This particular solver performs well for origami structural analysis based on the proposed N5B8 model and the nonlinear formulation (see Section 7.3.2).

7. Applications of bar and hinge models

The bar and hinge method provides a basic approach for global structural analysis of origami type systems. In this section, we show how the model can be used for both conventional structural analysis, as well as analysis techniques suited specifically to origami.

7.1. Kinematic folding of origami

The basic implementation of the bar and hinge model can be used to study the folding characteristics of an origami pattern or structure. As the panel and fold stiffness are treated separately in the model, it is possible to separate these behaviors and obtain information about the global folding characteristics from the stiffness matrix \mathbf{K} . Reducing the fold stiffness makes the kinematic folding the preferred (most flexible) method of deformation, but still allows for bending to occur along the panel diagonals. Here the fold lines taken to be much more flexible than the panels by using a L^* that is unrealistically high (e.g. 10^4).

Having defined the geometry of the origami pattern in a completely flat or three dimensional state, it is possible to explore folding motions by obtaining the eigenvalues λ_i and corresponding eigenmodes \mathbf{v}_i of the stiffness matrix as:

$$\mathbf{K} \mathbf{v}_i = \lambda_i \mathbf{v}_i. \quad (29)$$

The eigenvalues are arranged in an incremental order (i) and represent the elastic energy that would deform the structure into a shape represented by the corresponding eigenmode. The first six eigenmodes represent rigid body motion of the origami (three displacements and three rotations in space) and require no energy. We omit these six modes, and study the subsequent modes that require elastic deformation. The most flexible eigenmodes (lowest elastic energy) represent deformations where folding occurs along fold lines. As the eigenmodes become stiffer, folding of the panels also begins to occur, and the much stiffer eigenmodes include stretching and shearing of panels.

In Fig. 11(a) eigenmodes are used to find five rigid folding motions that can be performed on a Miura–ori patterned sheet. The top horizontal folds of the Miura sheet have a sector angle of $\alpha = 70^\circ$, while the bottom have $\alpha = 55^\circ$. The folding direction is shown by mountain and valley fold assignments, and all of the patterns can be reversed (i.e. valley folds become mountain and vice versa).

Eigenmode 9 represents the traditional folding motion for the Miura–ori sheet where all folds of the pattern are engaged. The other folding motions shown in eigenmodes 7, 8, 10 and 11 are also valid rigid folding motions where bending occurs only at the fold lines and the panels remain completely flat. These five eigenmodes are not a complete list of all feasible folding motions, and it is possible to obtain other valid patterns by linear combination of the eigenmodes (e.g. linear combination of modes 7 and 9 results in a different pattern). Eigenmodes 12 and higher require bending of the panels. When bending of the panels is considered, it is possible to find folding motions that do not follow rigid folding definitions.

The eigenmode analysis can also be used as a numerical method to perform the kinematic rigid folding of the origami. Using a numerical approach for folding is particularly useful for more complicated fold patterns that have non-repetitive fold vertices. The kinematic folding can be performed by iteratively updating the nodal locations by adding increments of a chosen eigenmode (and corresponding rigid folding pattern). The folding can be performed by correcting geometric errors using the Moore–Penrose pseudo-inverse (Tachi, 2009), or using Newton–Raphson iterations with a sufficiently small (e.g. 1/1000) increments of the eigenmode. The order of eigenvalues can change as the kinematic folding is performed, so it is necessary to track the eigenmode that corresponds to the chosen folding pattern. Tracking of the x^{th} eigenmode can be achieved by finding the i^{th} eigenmode that minimizes $|\mathbf{v}_i^{j+1} \pm \mathbf{v}_i^j|$, for the updated geometry at step $j + 1$. When performing the folding of the structure, it is assumed that the folds move freely, and the structure is unstressed after folding. In other words, forces and

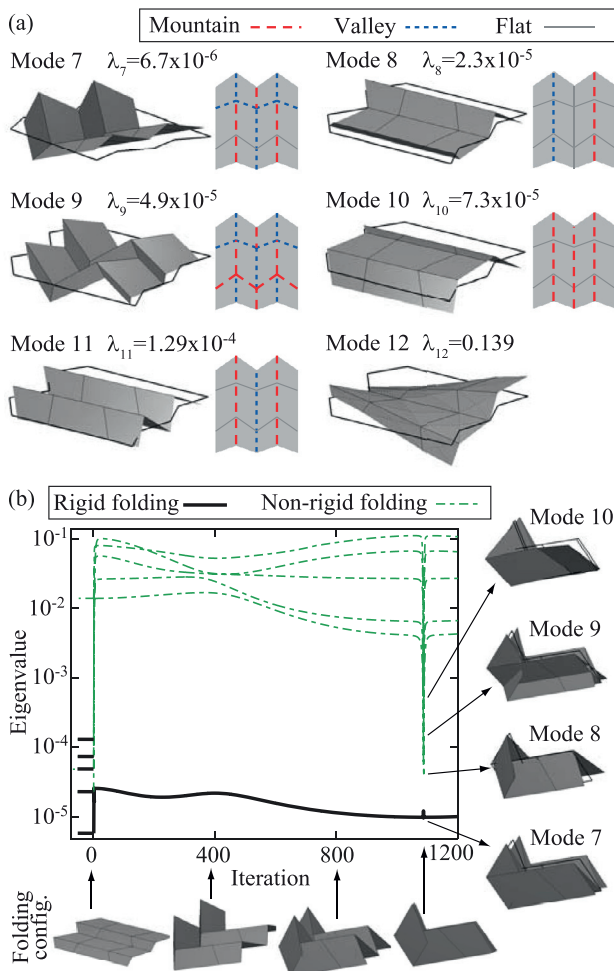


Fig. 11. Folding kinematics of a Miura-ori pattern. (a) Eigenmodes 7–11 of the flat sheet show five valid rigid folding motions with corresponding mountain and valley folds. The deformed modes are shown after one iteration of the folding algorithm, and thus they limit global deformations where bending of both folds and panels occurs. Although eigenmode 9 is typically the prescribed folding motion for Miura-ori sheets, it is not the only possible way in which the sheet can be folded. Eigenmode 12 represents a global bending of the sheet which is not a rigid folding mode (λ is orders of magnitude higher). (b) An iterative approach is used to fold the sheet based on the rigid folding motion in Mode 7. A jump in eigenvalues occurs after the first iteration because when the sheet starts folding into a rigid motion it can no longer deform globally with both fold and panel bending. The kinematics of Mode 7 are followed until the system reaches another flat state at ~ 1100 iterations. At that point other folding motions are enabled, some with self intersection.

stresses do not accumulate at the fold lines after the kinematic motion.

Fig. 11(b) shows the kinematic folding following the seventh eigenmode as a chosen fold pattern. At the first step there is a jump in eigenvalues. The value of λ_7 increases because the origami enters a rigid folding mode, and the seventh mode becomes self-restricting as global fold and panel bending is no longer possible in the newly folded configuration. Eigenvalues $\lambda_8 - \lambda_{11}$ increase by several orders of magnitude. The initial kinematic motions are no longer possible and the eigenmodes switch shape to new motions with global system bending (similar to the initial mode 12). The seventh mode does not become restricted, and the folding is iteratively performed until the origami reaches another flat state (flat folded at ~ 1100 iterations). At that point the eigenvalues drop again, and it is possible to explore other folding motions that are made available by the newly folded geometry. With the current

formulation the model does not account for self-intersection of the panel elements and can thus suggest unrealistic folding scenarios. In future work, the bar and hinge method may also be adopted to study the folding patterns and kinematics of *multi-DOF origami* that has more than four folds per vertex and can result in multiple folding motions (Xi and Lien, 2015).

The approach discussed in this section shares some similarity with the null space method used in Schenk (2011), and a Singular Value Decompositions (SVD) method introduced by Kumar and Pellegrino (2000). The eigenvalue approach can be more forgiving in detecting possible fold patterns, as the null space or SVD approach may not show a fold pattern if the updated geometry has a small error. The eigenmodes also simultaneously provide feedback into the global stiffness and behavior of the system (e.g. they show the most flexible method of folding), and can detect bifurcation points where the system can be reconfigured. Lastly, for multi-DOF patterns, the eigenmode analysis has the benefit of providing the most likely global deformation path. The eigenvalue method will globalize the deformation mode, whereas the nullspace and SVD will also show local deformations in multi-DOF patterns.

7.2. Informing structural behavior through eigenvalue analyses

The eigenvalues and eigenmodes of the stiffness matrix discussed in Section 7.1 can also provide significant information about the structural characteristics of the system. For example, Schenk and Guest (2011) use these analyses to evaluate how the structural behavior of Miura-ori and egg-box patterns is affected by changing the relative stiffness between panel bending and fold lines. Alternatively, it is possible to incorporate the mass matrix of the structure (\mathbf{M}), and use the linear dynamics system of equations

$$\mathbf{K}\mathbf{v}_i = \lambda_i \mathbf{M}\mathbf{v}_i, \quad (30)$$

to find λ_i and \mathbf{v}_i . In this work the mass matrix \mathbf{M} is constructed by distributing 1/5 of the panel mass to each of the panel's nodes, however more advanced shape function approaches can be used to distribute the mass of the panel. Including mass in the analysis can be beneficial for performing scale dependent studies, comparing different systems, and exploring the dynamic properties of the system.

In Fig. 12 we use the eigenvalues and eigenmodes that incorporate mass to compare the behavior between an eggbox pattern and an origami tube. The eggbox pattern is curved with repetitive panels that have sector angles $\alpha = 62.9^\circ, 117.1^\circ, 69.3^\circ, 110.3^\circ$ and the left panel dimension is a unit value of 1 (Xie et al., 2015). The panels have a thickness of $t = 0.01$ ($L/t \approx 100$), and mass of $\rho = 1$. The model uses a Young's Modulus $E = 10^6$ and fold lines are defined with $L^* = 40$. The magnitude of the eigenvalues 7–14 for the eggbox are relatively low, indicating that the most flexible ways to deform the structure (folding, bending, and twisting) require only deformation of the fold lines and panels. As the structure is extended, mode switching takes place, meaning that depending on the configuration, it may be easier to deform the structure in different ways.

In Fig. 12(b) the eggbox is closed on the bottom to create a rigid foldable tube (Tachi, 2009c) that has a symmetric cross-section with all edges having a dimension of 1. Because mass is used with this analysis, it is possible to compare the results between the eggbox and the tube. When additional panels are added, both the stiffness and mass scale linearly with the change in material. Thus any change in the eigenmodes and eigenvalues can be attributed to the change in geometry. When the second part of the tube is added, the magnitude of the seventh eigenvalue does not change drastically, however, mode switching no longer occurs, and the lowest eigenmode corresponds only to the folding and unfolding motion. Deforming the structure in bending and twisting is stiffer than for

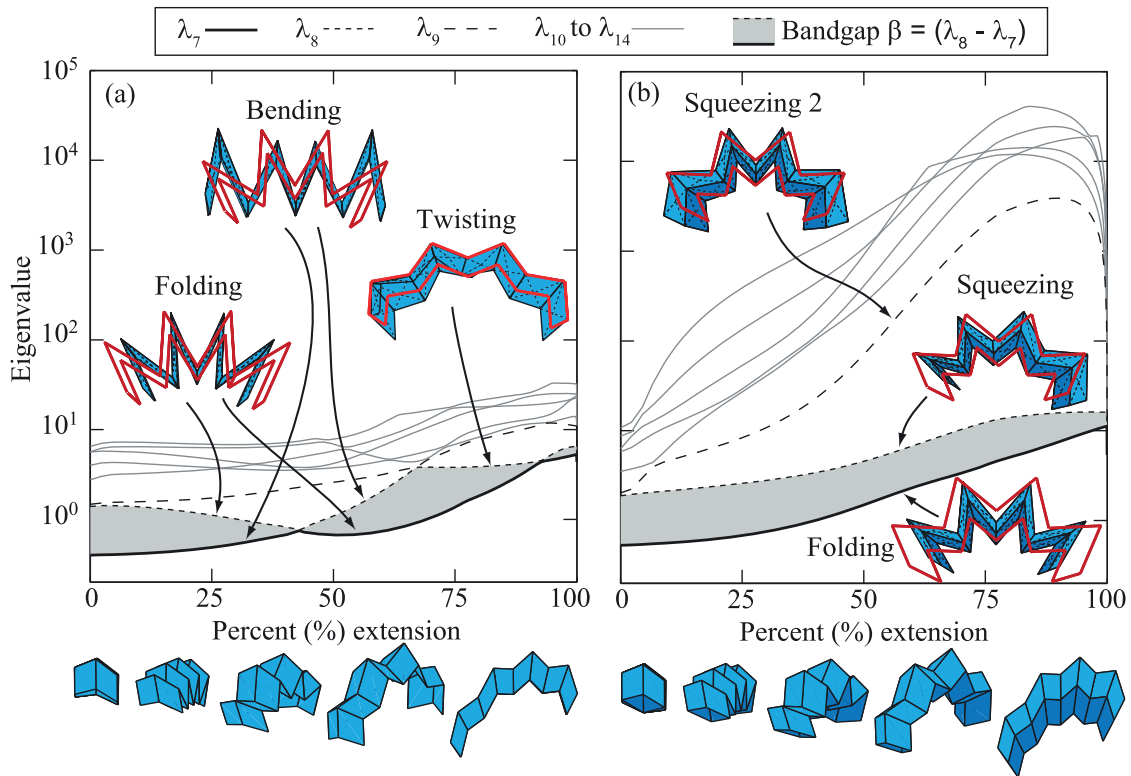


Fig. 12. Eigenvalues vs. configuration (% extension) of (a) a curved eggbox form and (b) a tube with the top section identical to (a). The deformation modes of the eggbox are more flexible than the tube and switch at different configurations. The tube has a continuous bandgap for different configurations indicating that it requires less energy to deploy the structure than to deform it in other ways (e.g. twisting).

the eggbox, and the eighth eigenmode becomes a squeezing type of motion where one side folds and the other unfolds. The ninth and subsequent eigenvalues are substantially stiffer and engage the panels in stretching and shear. A bandgap ($\beta = \lambda_8 - \lambda_7$) separates the seventh and eighth eigenvalues throughout the extension of the structure. This separation means that it is always more flexible for the system to be deployed than to be deformed in another fashion. Previous work in Filipov et al. (2015) showed that coupling multiple tubes can be used to substantially increase the structural bandgap. The system becomes easy to deploy yet it is stiff in all other directions and can be used as a cantilever. Analyzing the bandgap between the seventh and eighth eigenvalues is particularly important for origami, because it informs whether the origami is capable of deploying easily per design or if other motions are possible.

The bar and hinge model and Eq. (30) could also be used to find the circular natural frequency ($\omega_i = \sqrt{\lambda_i}$) of the structure to investigate the dynamic characteristics and behavior of the system (e.g. if they are to be used as mechanical systems subject to vibration).

7.3. Static analyses of origami systems

Static analyses are useful when a specific application of origami is explored. For these types of analyses we provide supports that prevent rigid body motions. Loads are applied at unrestrained nodes and a deformed shape of the structure is obtained. It is also useful to characterize the stiffness of different origami structures for loads applied in the three Cartesian coordinates.

7.3.1. Infinitesimal deformation analysis

In this section, we present a cantilever analysis of an eight-sided reconfigurable polygonal tube presented in Filipov et al. (2016b). We perform the analysis on the structure with the

N5B8 model, and compare the results to a discretized FE model. Both models are defined with unit dimensions (see Filipov et al., 2016b for the specific geometric definitions of the tubes). The cross-section edges for the upper section of the polygonal tube have slopes of $[\theta_a, \theta_b, \theta_c] = [30, 90, 125]^\circ$, and lengths of $[b_{U1}, a_{U1}, b_{U2}, c_{U1}] = [0.5, 0.7, 0.5, 1]$. The tube is ten segments long, and is created with constant projection of $\phi = 60^\circ$ and $l = 1$. The panels have a thickness of $t = 0.01$ units ($L/t \approx 50 - 100$), Poisson's ratio of $\nu = 1/3$, Young's Modulus of $E = 10^6$, and fold lines are defined with $L^* = 40$. The polygonal tube can reconfigure to have six different cross-sectional shapes (I - VI).

One end of the cantilever is fixed and a uniformly distributed load is applied on the other end. We perform static, linear elastic, small displacement analyses of the structures when they are deployed to 95% extension. Fig. 13(a) and (b) show the displaced shapes obtained with the N5B8 and FE models when a load is applied in the Y direction and the structure is in configuration I. We find the characteristic stiffness for each of the six possible configurations (I - VI), when the tubes are deployed to 95% extension. The load is applied in the YZ plane, and the cantilever stiffness K_{YZ} is calculated as the load is rotated.

The radial plots show that the cantilever stiffness depends on the direction of loading, and that the tube geometry has a high influence on the anisotropy of the tube structures. The N5B8 and the FE model provide similar displaced shapes and radial plots depicting the K_{YZ} stiffness. However, the N5B8 model overestimates the global stiffness of the polygonal tube by as much as 160%. This significant difference is partly due to the overestimation in shear stiffness of the origami panels, and also because the N5B8 model cannot capture localized deformations. Nonetheless, the global influence of geometry is accurately captured by the bar and hinge model, and it provides a good qualitative and comparative analysis of different origami geometries.

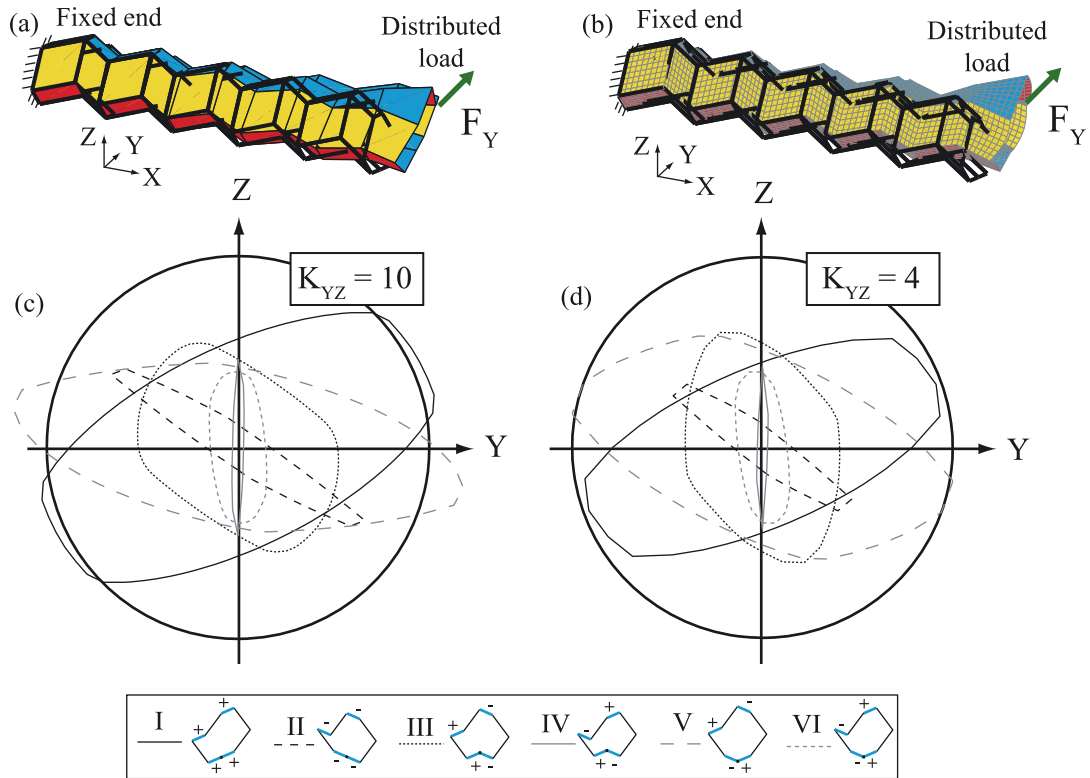


Fig. 13. Structural analysis of cantilevered reconfigurable tube. (a) and (c) are performed with the N5B8 model while (b) and (d) are performed with a discretized FE model. The displaced shapes presented in (a) and (b) appear similar but are scaled to have the same maximum displacement and do not represent stiffness. (c) and (d) are the tube stiffness for different loading directions in the $Y - Z$ plane represented as a radial plot. The stiffness for the six possible tube configurations (I - VI) are shown when the system is at 95% extension. The N5B8 and FE plots show similar behaviors but the stiffness estimated by the N5B8 model is higher.

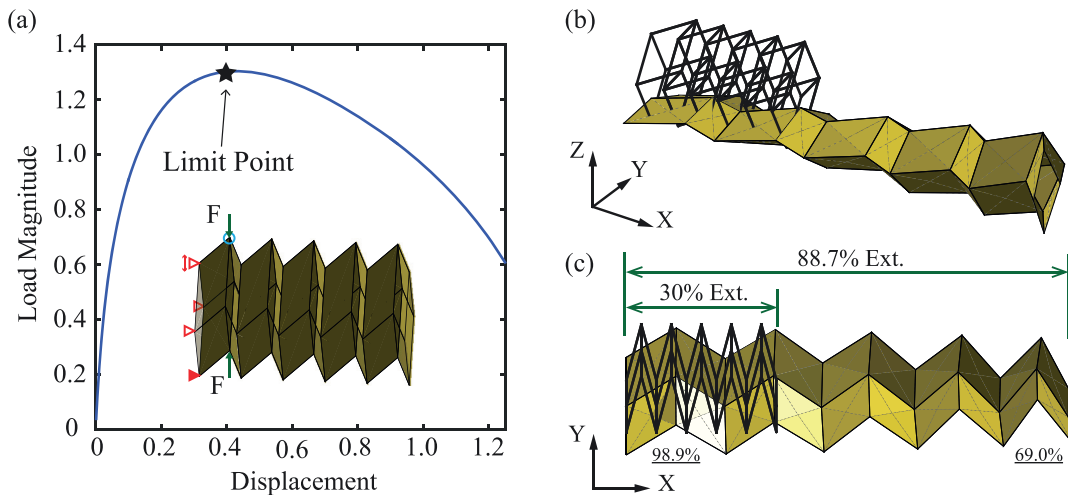


Fig. 14. Large displacement analysis of a Miura-ori tube structure. (a) The load-displacement curve. The initial geometry and boundary conditions are shown by the inset. The left end of the tube is supported: the bottom node is fully pinned in three directions; the top node is only allowed to slide in the Z direction; the two middle-height nodes are only restricted in the X direction. The displacement is measured as the downward Z movement of the node marked with a circle. (b) An isometric view of the deformed structure. The thick line frame shows the original geometry. (c) A top view of the deformed shape. The unit sections are deployed non-uniformly under the given actuation.

7.3.2. Large deformation analysis

The bar and hinge model can also capture large global deformations of origami structures. For example, when actuating a Miura-ori tube from one end, due to the flexibility of panels, the panels experience bending in a non-uniform fashion, and only part of the tube moves (similar to squeezing in Fig. 12(b)). The geometry of a straight tube is shown in Fig. 14, featured with uniform $\alpha = 60^\circ$ sector angled panels. The model is defined similar to the previous example ($t = 0.01$ ($L/t \approx 100$), $\nu = 1/3$, $E = 10^6$), except that

here we take $L^* = 10$. The formulation for large displacement analysis is presented in Section 6. To conduct the nonlinear analysis, we use the MGDCM as the solver (Leon et al., 2014). The tube is supported at the left end: the bottom node is fully pinned in the three directions; the top node is only allowed to slide in the Z direction; the two middle-height nodes are only restricted in the X direction, so they can move freely in the $Y - Z$ plane. The external forces are applied in the Z direction as shown in Fig. 14. A squeezing type motion occurs where the side of the tube that is

restrained folds down to approach a flattened sheet, whereas the other end deforms substantially less. This behavior is due to flexibility of the panels. After passing the limit point shown on the force-displacement curve, this deformation process shows a softening behavior where the stiffness decreases. A Miura-ori tube with fully rigid panels would deploy uniformly (i.e. rigid origami with only one degree of freedom for rigid folding).

7.4. Characteristics of origami inspired materials

Mechanical analysis of origami inspired materials is often performed as local unit cell exploration aimed to characterize the mechanical properties of the system. When a larger material specimen is to be investigated the bar and hinge model can be a useful tool that can characterize behavior and explore geometric and other specimen variations. The mechanical properties of the origami system depend on the fold pattern, fold angles, material properties, material thickness and other properties which can be easily scaled and parametrically explored using the bar and hinge model. We perform a static analysis on the assemblage of interleaved tube cellular material (Cheung et al., 2014) by applying a uniform load at both the bottom and top of the system. The characteristic stiffness for each direction is calculated based on the mean displacement of the loaded surfaces. Fig. 15 shows that the stiffness of the assemblage can be tuned by changing the configuration. The maximum stiffness in the X and Y directions is obtained when the structure becomes flattened in a parallel plane (e.g. in the X–Z plane for X loads). In the Z direction the stiffness has three maxima, with the intermediate one occurring at a deployed symmetric state. We also show that the Poisson's ratio in the three Cartesian directions can be tuned with reconfiguration. We calculate the Poisson's ratio as a resultant of the Y displacement with respect to a load applied in the X direction as $\nu_{yx} = -(dy/l_y)/(dx/l_x)$, where dy and dx are the displacements in the two directions and l_y and l_x are the corresponding initial lengths of the metamaterial. Due to the kinematic deformation motion of the origami assemblage, the material can take on Poisson's ratios that are much larger or smaller than conventional materials (Fig. 15(c) and (d)).

8. Summary and discussion

This section summarizes the properties of bar and hinge models in general and, in particular, the properties associated with the N5B8 model. Afterwards, the limitations of those models are also presented.

8.1. Properties of bar and hinge models

- The bar and hinge models are simple to understand, implement, modify and use. This makes them valuable to the growing community of origami researchers and enthusiasts.
- The models distill structural behavior of origami into three intuitive components: (1) bending of creases, (2) bending of flat panels, and (3) stretching/shearing of the material. This makes the model and methodology especially useful when describing structural behaviors of different origami systems (see Section 7).
- The bar and hinge models use few nodes per each panel allowing for more simplicity and efficiency than a discretized FE approach.
- The speed and versatility of the models makes them suitable for various extensions such as: (i) Parametric variations for geometric design; (ii) Optimization of cellular origami type structures; (iii) Large displacement simulations; (iv) Exploring the effect of different nonlinear fold line models.

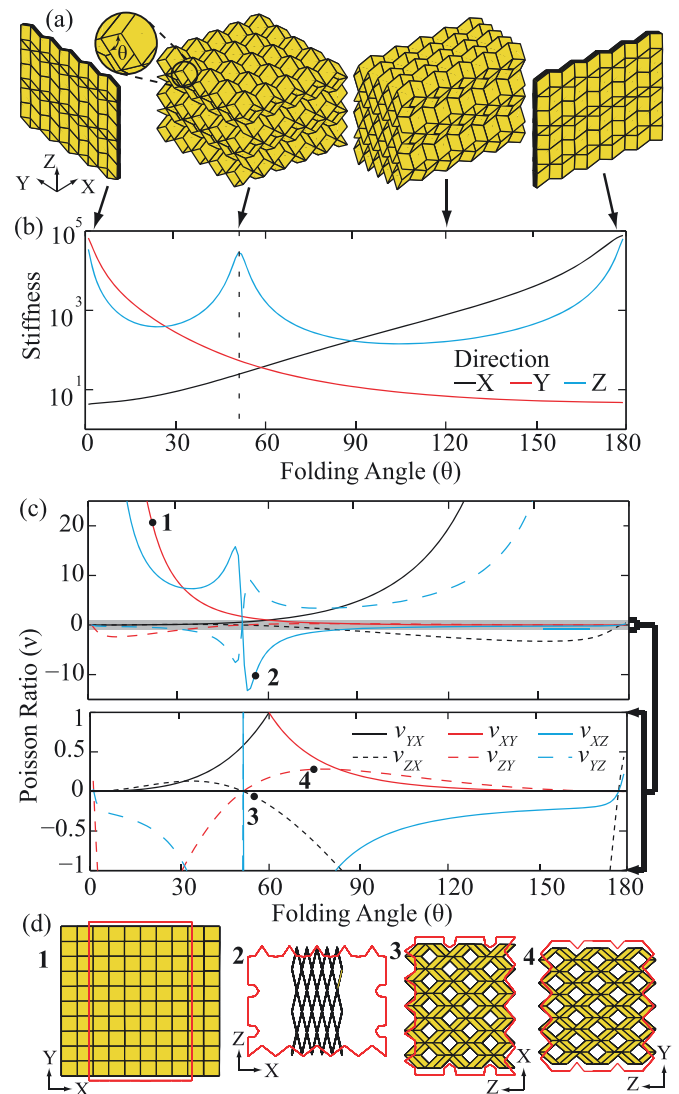


Fig. 15. Structural linear elastic analysis of interleaved tube cellular material (Cheung et al., 2014). (a) Four folding states of the cellular material; the system can fold flat in both the X and Y directions. (b) Stiffness of the material in three directions at different folding states. (c) The analytical Poisson's ratio (ν) simulated with the bar and hinge model. (d) Four deformed states of the structure when compressed at different configurations and in different directions. The undeformed outline is shown with a red line. Cases 1 and 4 have positive ν , Case 3 has $\nu \approx 0$ and Case 2 has a negative ν . These results are based on infinitesimally small displacements, and would differ for large displacement simulations. (For interpretation of the references to colour in this figure legend, the reader is referred to the web version of this article.)

8.2. Properties of the specific N5B8 model

- The model is simple and efficient while allowing for a surprising level of detail and accuracy.
- In-plane behaviors exhibit symmetry and isotropy which is not possible with N4B5 models.
- The model can approximate in-plane stretching and shearing for both regular and skewed panels. Although shear stiffness is overestimated, the model behaves similar to expected trends when skew is incorporated.
- The N5B8 model can approximate deformed shapes reasonably well when bending of both panels and fold lines occurs. The model removes ambiguity between panel and fold line bending that occurs with N4B5 and N4B6 models.
- Mass can be distributed more realistically in the N5B8 model than in the N4B5 and N4B6 models.

- The N5B8 model is scalable as it includes length and thickness (t) to define the stiffness and mass of the system.

8.3. Findings applicable to the bar and hinge and other origami models

- Panel bending stiffness can be defined to scale based on the width to thickness ratio as $(D_S/t)^{1/3}$ and with the bending modulus of the sheet k (suggested by Lobkovsky et al. (1995)).
- The out-of-plane panel bending stiffness for small displacements is highly dependent on panel geometry and skew ($\Sigma\alpha$). Skewed or elongated panels tend to be more stiff than square panels as they restrict double curvature over the surface.
- Alternative formulations for panel bending may be used for large displacement bending of panels, because the stiffness scales with $\theta_B^{4/3}$ (behavior first discussed by Lobkovsky et al. (1995)). The panel geometry does not significantly influence stiffness for large displacements.
- The local fold line stiffness can be defined to scale with the fold length L_f , the bending modulus of the sheet k , and a length scale parameter as $1/L^*$, (first suggested by Lechenault et al. (2014)). The length scale parameter is believed to scale with thickness, but also depends strongly on material, fabrication, and geometric characteristics of the fold.
- The global fold line stiffness should be modeled as a series of the local fold stiffness (K_f) and the adjacent panel stiffness (K_m) as $K_F = 1/(1/K_f + 1/K_m)$.
- For origami structures fold bending is expected to dominate, and a panel to fold stiffness ratios of $K_B/K_F = 1/3$ to 20 are expected to be realistic.

8.4. Limitations

- The bar and hinge model cannot capture localized effects accurately, such as stress concentrations at vertices due to thickness of the material.
- Stiffness for shearing of the panels is overestimated in comparison to the stretching and bending deformations.
- The bar and hinge models can currently only model quadrilateral and triangular panels. New formulations for both in-plane and out-of-plane behaviors will be needed for arbitrary polygonal panel geometries.
- Bar and hinge models are not currently available in easy to use software packages and are thus not easily accessible for widespread use.

9. Conclusions

This paper discusses bar and hinge models for the mechanical and structural simulation of origami type systems. We introduce a bar and hinge model where five nodes and eight bars (N5B8 model) are used to simulate the in-plane stiffness of origami panels. This orientation of bars allows for the bending of the panels along the diagonals, which is a characteristic behavior of origami in large deformation. Rotational hinges are used to simulate the out-of-plane bending of the panels, as well as the moment-rotation behavior of prescribed fold lines. The model parameters incorporate realistic material characteristics, and the model is formulated to provide a scalable, isotropic, and realistic system behavior. The influence of panel geometry on the origami stiffness, and a study on fold line stiffness characteristics are also presented and implemented.

Bar and hinge models have various applications for the characterization and design of origami type structures and systems. Folding pattern characteristics and kinematic rigid folding can be performed using eigenvalues and eigenmodes of the stiffness matrix.

When mass is incorporated with the eigen-analysis, it can provide a scalable basis for comparing the mechanical characteristics of origami structures. Static analyses can be used for stiffness characterization of origami inspired deployable structures or mechanical metamaterials. We show the model's capabilities for studying large displacements and instabilities that are possible with the thin sheet systems. The bar and hinge model cannot capture localized phenomena of origami, but has the benefits that it is versatile, efficient, and adaptable for a wide range of applications. The bar and hinge model can be a useful analytical and design tool that facilitates practical application of origami in science and engineering.

Acknowledgments

The authors acknowledge partial support by the [National Science Foundation](#) (NSF) through grant no. [CMMI 1538830](#), and the NSF Graduate Research Fellowship. The research was also partially supported by the Japan Society for the Promotion of Science Fellowship; the China Scholarship Council; the Raymond Allen Jones Chair at the Georgia Institute of Technology; and the Japan Science and Technology Agency Presto program. We thank Professor Gregory J. Rodin, from the University of Texas at Austin, for helpful discussions. Prof. William "Bill" McGuire's work paved the way for many developments in the field and thus the presentation in this paper is inspired from the fundamental work done by him and his colleagues. In fact, if Bill were here today, we believe that he would be pleased to see new application areas of matrix structural analysis, such as our bar and hinge models for scalable analysis of origami.

Appendix A. Stiffness characteristics for thin sheet bending

This appendix presents stiffness scaling characteristics for the bending of thin restricted sheets. The scaling properties are evaluated through parametric studies of the FE model presented in [Section 4.2](#). First we verify and compare with existing findings for large deformation bending introduced by [Lobkovsky et al. \(1995\)](#), and subsequently we explore the influence of the panel geometry

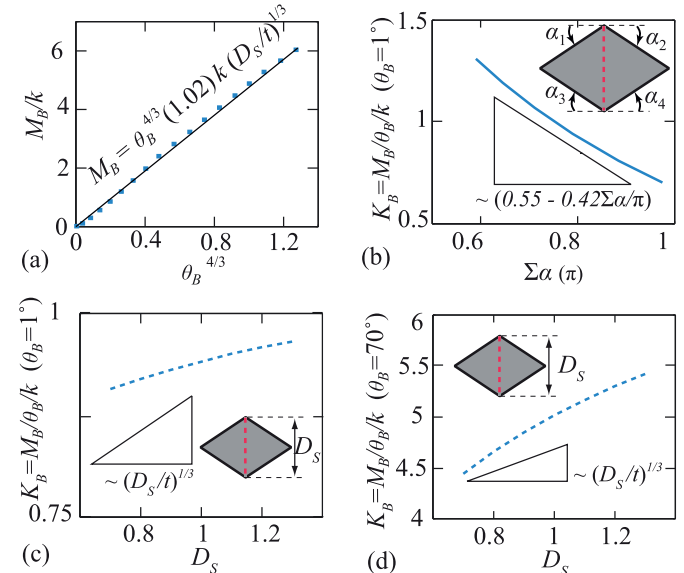


Fig. A.16. Some of the scaling relations that influence thin sheet bending. (a) The normalized bending moment M_B/k scales roughly with $\theta_B^{4/3}$ from small to large displacements. (b) For small displacements ($\theta_B = 1^\circ$) the normalized bending stiffness (K_B) scales primarily with the geometric parameter $\Sigma\alpha = \alpha_1 + \alpha_2 + \alpha_3 + \alpha_4$. Small displacement (c) and large displacement (d) scaling of the normalized bending stiffness (K_B) with respect to the length of the short diagonal (D_S).

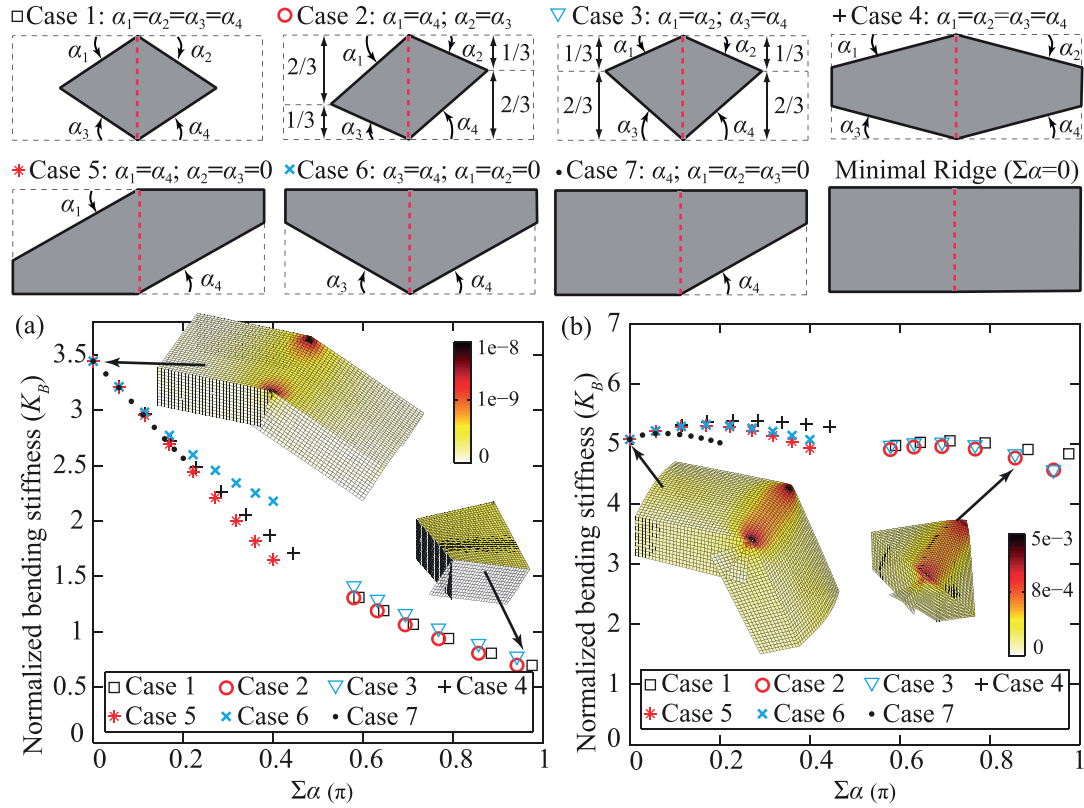


Fig. A.17. Influence of panel skew on bending stiffness. The panels with different skewed configurations are quantified by $\Sigma\alpha = \alpha_1 + \alpha_2 + \alpha_3 + \alpha_4$. Normalized bending stiffness vs. panel corner geometry ($\Sigma\alpha$), for (a) small displacement bending ($\theta_b = 1^\circ$) and (b) large displacement bending ($\theta_b = 70^\circ$). Skew has an influence on the bending stiffness for small displacements, but not for large displacements.

on the bending stiffness. Fig. A.16(a) shows that as bending transition from small to large displacements, the bending moment scales reasonably well with $\theta_b^{4/3}$. This behavior differs from a linear hinge and, in contrast, the restrained panel becomes stiffer with larger bending angles. When considering only small deformations of the panel, Fig. A.16(b) shows that the bending stiffness scales with a geometric parameter $\Sigma\alpha$ (discussed in more detail below). Some of the stiffness scaling characteristics are similar for both small and large deformations. In particular, Fig. A.16(c) and (d) show that bending moment scales roughly with $k(D_S/t)^{1/3}$ where k is the bending modulus of the sheet, defined as $k = Et^3/12(1 - \nu^2)$. Although not exact, our results show similar scaling trends of $(D_S/t)^{1/3}$ that were presented both analytically and numerically by Lobkovsky et al. (1995).

Beyond verifying previous scaling relationships, this appendix also explores the influence of the panel geometry and skew on the bending stiffness. Analyses were performed on panels with different geometries and a constant short diagonal D_S . Fig. A.17, shows seven different geometries, with Cases 1–3 using a rhombus geometry similar to Fig. 7, and Cases 4–7 using a modified geometry derived from the *minimal ridge* case where $\Sigma\alpha = 0$ (Witten, 2007). The geometric parameter $\Sigma\alpha$ for Cases 1–3 is modified by changing the length of the long diagonal D_L . Cases 4–7 are modified by increasing the angles α starting from the minimal ridge case. The bending stiffness for small displacements is highly dependent on the corner geometry $\Sigma\alpha$. We note that this parameter ($\Sigma\alpha$) is effective at representing the panel stiffness of panels with vastly different geometries.

An elongated panel with $\Sigma\alpha = 0.6\pi$ ($D_L \approx 2D_S$) would have about double the stiffness of a square panel with $\Sigma\alpha = \pi$. When the panel is a square it experiences double curvature with uniform bending energy over the entire area of the panel. The system is

stiffer when the panel shape is more skewed, elongated, or the corners of the short diagonal are more obtuse (e.g. Case 3 or Case 6). The stiffer cases occur because bending becomes restricted at the obtuse corners and double curvature is limited. For the large displacement cases the skew and geometric parameter $\Sigma\alpha$ do not have a significant effect. In these cases bending is restricted to the short diagonal of the panel, thus the elongation and skew of the panel have little effect on the global stiffness. These observations that boundary conditions and geometry are not of significant influence for large displacement cases were also noted in previous research (Di Donna and Witten, 2001; Witten, 2007). More details on the scaling relations of thin sheet origami panels, and how skew and geometry affect the bending energy in these systems can be found in Filipov (2016).

Appendix B. Stiffness characteristics of creased fold lines

In the modeling of origami fold lines, a length scale factor L^* (in units of length) is often used to define the relative stiffness of the fold based on the material, fabrication, and geometric properties. To better understand realistic values of L^* this appendix presents a study of published experimental research on creased fold lines, as summarized in Table 1. The experiments consist of the following: 1 - Beex et al. (2009); 2 - Huang et al. (2014); 3 - Lechenault et al. (2014); 4 - Mentrasti et al. (2013); 5 - Nagasawa et al. (2001); 6 - Nagasawa et al. (2003); 7 - Nagasawa et al. (2008); 8 - Pradier et al. (2016); and 9 - Yasuda et al. (2013). Table 1 documents the material properties, testing direction for the paper based samples, the creasing type and the general bending behavior. Several of the experiments crease and cycle the fold before testing (3,8,9) and in one case the thickness is partially cut or a dash cut is performed through the thickness (4ab). In the remainder of the cases

Table 1
Experimental results of fold line testing.

#	Paper	Material	Crease type	Direction	E (GPa)	t (mm)	K_c/L_F (Nm/m/rad)	L^* (mm) ^c	Comment
1	Beex et al. (2009)	Laminated paperboard	Die crease - V	MD	1.3 ^a	0.9	1.72-11.5	7.7 - 52	Elasto-plastic response affected by creasing depth.
2	Huang et al. (2014)	Multi-ply layered paperboard A	Die crease - V	MD	4.4 ^a	0.383	0.9 - 2.1	11-25	Elasto-plastic response affected greatly by creasing depth. The creasing direction (MD/CD) and the material properties of different plies (samples A,B,C) can influence behavior.
			Die crease - V	CD	1.5 ^a	0.383	0.32 - 1.1	7.2-25	
		Multi-ply layered paperboard B	Die crease - V	MD	4.5 ^a	0.39	0.7 - 1.8	14-36	
			Die crease - V	CD	2.6 ^a	0.39	0.5 - 1.4	10-29	
3	Lechenault et al. (2014)	Mylar sheets	Folded by hand and weight - C	N/A	4	0.13	0.029	28	Essentially elastic response for large angle variations. Behavior depends on origami length scale.
				N/A	4	0.35	0.27	60	
				N/A	4	0.5	0.5	94	
				N/A	4	0.4 - 0.44	0.041-0.095	222-667	
4	Menttrasti et al. (2013b)	Paperboard	a. Cut - C/V b. Dash cut - C/V c. Die crease - V	U	3.5 ^b	0.4	0.38-0.73	29-55	Essentially elastic response. Elasto-plastic response. Response can vary significantly.
				U	3.5 ^b	0.4 - 0.44	0.16-0.69	30-133	
				U	3.5 ^b	0.44	2.6-3.7	7.6-11	
5	Nagasawa et al. (2001)	Paperboard	Die crease - V	MD	3.5 ^b	0.46	0.5-5.4	5.9-64	Elasto-plastic response, peak strength was affected by creasing but stiffness was not.
				CD	3.0 ^b	0.46	0.3-2.9	9.5-91	
7	Nagasawa et al. (2008)	Paperboard	Die crease - V	MD	1.6	0.37	1.6-4.7	1.6-4.8	Elasto-plastic response affected greatly by creasing depth. Aluminum coating increases stiffness in non creased cases.
				CD	1.05	0.37	0.7-2.8	1.8-7.1	
		Paperboard coated with aluminum foil	Die crease - V	MD	1.6	0.37	1.6-5.2	1.6-4.8	
			Die crease - V	CD	1.05	0.37	0.7-3	1.7-7.1	
8	Pradier et al. (2016)	ECF woodfree pulp uncoated paper	Folded by hand and weight - C	MD/CD/45 °	4 MD	0.129	0.042	19	Essentially elastic response with stiffening when fold opens. Direction (MD/CD) does not influence behavior significantly.
9	Yasuda et al. (2013)	Paper	C	U	2.9 ^a	0.27	0.106	50	Linear behavior with stiffening when fold reaches closed state.

Notes: Crease type: V - virgin folding of material; C - material is pre-folded and cycled or pre-cut; MD - Machine (grain) Direction; CD - Cross-machine (parallel) Direction; U - Unknown information.

^a Value interpolated from results presented in paper.

^b Value assumed for typical paper/paperboard.

^c Except for ref. #3, the authors computed the L^* values.

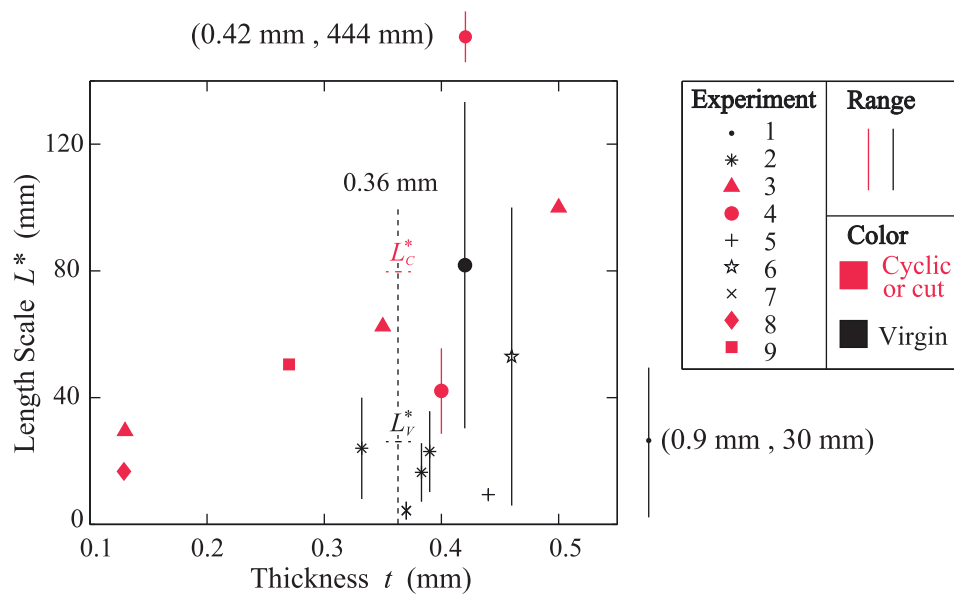


Fig. B.18. The length scale L^* with respect to the thickness for the experiments in Table 1. The red (gray in B&W) points are cases where the crease is cycled or pre-cut. The black points represent cases where a virgin loading is applied to a die crease. The distribution of L^* from the different experiments does not show a strong correlation with thickness, and likely material, fabrication and other properties have a more significant influence. We show representative values of the length scale for the virgin (L_V^*) and the cyclic (L_C^*) tests for a material thickness of 0.36 mm. Two outliers from the experiments (experiment 1 and 4a) are represented off the plot with the numerical value of the central points (t, L^*). (For interpretation of the references to colour in this figure legend, the reader is referred to the web version of this article.)

(1,2,4c,5,6,7), a die crease mechanism is used and a virgin loading (folding) of the sample is tested. From the experimental results, we find the initial stiffness of the fold line with respect to the bending angle (in radians) and normalize by the fold length to obtain a normalized stiffness K_c/L_F (in units of Nm/m/rad). Most cases where a virgin loading is performed exhibit a highly non-linear elasto-plastic type of response, and for our calculations we only use the initial stiffness at the beginning of the experiment. For each set of experiments a range of values of the length scale are calculated as $L^* = L_F k / K_c$. The bending modulus (k) uses thickness of the tested material (t) and the recorded elastic modulus (E) where available. The value of E is assumed for typical materials if not available from the experimental data, and we assume that the Poisson's ratio is $\nu = 1/3$ for all cases. In some studies the range in L^* resulted from sample variability (4,5,8), while in other studies the range in L^* can be attributed to the creasing penetration depth (1,2,6,7). Cases with deeper creasing typically result in more damage to the material and a more flexible fold line (higher values of L^*); experiments 1, 5, 6, and 7 contain some samples where no creasing is performed.

To show the variability in fold stiffness, in Fig. B.18 we plot the length scale L^* with respect to the thickness for the nine tested specimens. The cases where cyclic loading or cutting is performed tend to have higher length scales, indicating a more flexible fold line. The cases where only the virgin loading is recorded (1,2,4c,5,6,7) would likely have much higher length scales (be more flexible) if the fold is cycled or the entire loading curve is considered. The results from Lechenault et al. (2014) (tests 3) show a trend that L^* increases with thickness, however, in general it appears that the material, fabrication, and fold properties have a much greater effect on L^* . Consequently, we do not attempt to fit the data. To provide a point of reference, for a material thickness of 0.36 mm we pick two points to show: (1) flexible folds typical for origami with cutting and cyclic loading ($L_C^* = 80$ mm), and (2) a high stiffness estimate of folds with little creasing or virgin loading ($L_V^* = 25$ mm). Future experiments can provide improved estimates for the scaling of L^* with respect to thickness, and other fold characteristics.

References

- Abaqus FEA, 2010. Version 6.10 documentation. Dassault Systemes Simulia Corp. Providence, RI, USA.
- Beex, L.A.A., Peerlings, R.H.J., folding, A.e., and, c. s. o.l.p.c., 2009. Int. J. Solids Struct. 46 (24), 41924207.
- Belcastro, S.M., Hull, T.C., 2002. Modeling the folding of paper into three dimensions using affine transformations. Linear Algebra Appl. 348, 273–282.
- Bridson, R., Marino, S., Fedkiw, R., 2003. Simulation of clothing with folds and wrinkles. In: ACM SIGGRAPH/Eurographics, pp. 28–36.
- Brunck, V., Lechenault, F., Reid, A., Adda-Bedia, M., 2016. Elastic theory of origami-based metamaterials. Phys. Rev. E 93, 033005.
- Chen, Y., Peng, R., You, Z., 2015. Origami of thick panels. Science 349, 396–400.
- Cheung, K.C., Tachi, T., Calisch, S., Miura, K., 2014. Origami interleaved tube cellular materials. Smart Mater. Struct. 23 (9), 094012.
- Del Grosso, A.E., Basso, P., 2010. Adaptive building skin structures. Smart Mater. Struct. 19, 124011.
- Demaine, E.D., Demaine, M.L., Hart, V., Price, G.N., Tachi, T., 2011. (Non)existence of pleated folds: how paper folds between creases. Graphs Comb. 27 (3), 377–397.
- Di Donna, B.A., Witten, T.A., 2001. Anomalous strength of membranes with elastic ridges. Phys. Rev. Lett. 87 (20), 206105.
- Dudte, L.H., Vouga, E., Tachi, T., Mahadevan, L., 2016. Programming curvature using origami tessellations. Nat. Mater. 15 (5), 583588.
- Edmondson, B.J., Lang, R.J., Magleby, S.P., Howell, L.L., 2014. An offset panel technique for rigidly foldable origami. In: Proc. ASME IDETC/CIE 2014. V05BT08A054
- Evans, A.A., Silverberg, J.L., Santangelo, C.D., 2015. Lattice mechanics of origami tessellations. Phys. Rev. E 92, 013205.
- Filipov, E.T., 2016. Tailoring Stiffness of Deployable Origami Structures. Ph.d. thesis. Univ of Illinois at Urbana Champaign, Urbana, IL.
- Filipov, E.T., Tachi, T., Paulino, G.H., 2015. Origami tubes assembled into stiff, yet reconfigurable structures and metamaterials. Proc. Natl. Acad. Sci. USA 112 (40), 12321–12326.
- Filipov, E.T., Tachi, T., Paulino, G.H., 2016. Toward optimization of stiffness and flexibility of rigid, flat-foldable origami structures. In: Miura, K., Kawasaki, T., Tachi, T., Uehara, R., Lang, R.J., Wang-Iverson, P. (Eds.), In Origami 6, Proc. 6th Int. Meeting on Origami Science, Mathematics, and Education. American Mathematical Society, p. 409419.
- Filipov, E.T., Tachi, T., Paulino, G.H., 2016b. Origami tubes with reconfigurable polygonal cross-sections. Proc. R. Soc. A 472 (2185), 20150607.
- Fuchi, K., Buskohl, P.R., Bazzan, G., Durstock, M.F., Reich, G.W., Vaia, R.A., Joo, J.J., 2015. Origami actuator design and networking through crease topology optimization. J. Mech. Des. 137 (9), 091401.
- Fuchi, K., Buskohl, P.R., Bazzan, G., Durstock, M.F., Reich, G.W., Vaia, R.A., Joo, J.J., 2016b. Design optimization challenges of origami-based mechanisms with sequenced folding. J. Mech. Rob. 8 (5), 051011.
- Fuchi, K., Buskohl, P.R., Joo, J.J., Reich, G.W., Vaia, R.A., 2016. Numerical analysis of origami structures through modified frame elements. In: Miura, K., Kawasaki, T., Tachi, T., Uehara, R., Lang, R., Wang-Iverson, P. (Eds.), Origami 6, Proc. 6th Int.

- Meeting on Origami Science, Mathematics, and Education. American Mathematical Society, pp. 385–395.
- Gattas, J.M., Wu, W., You, Z., 2013. Miura-base rigid origami: parameterizations of first-level derivative and piecewise geometries. *J. Mech. Des.* 135 (11), 111011.
- Gattas, J.M., You, Z., 2015. The behavior of curved-crease foldcores under low-velocity impact loads. *Int. J. Solids Struct.* 53 (15), 80–91.
- Giampieri, A., Perego, U., Borsari, R., 2011. A constitutive model for the mechanical response of the folding of creased paperboard. *Int. J. Solids Struct.* 48 (16–17), 2275–2287.
- Guest, S.D., Pellegrino, S., 1994. The folding of triangulated cylinders, part II: the folding process. *J. Appl. Mech.* 61, 778–783.
- Hanna, B.H., Lund, J.M., Lang, R.J., Magleby, S.P., Howell, L.L., 2014. Waterbomb base: a symmetric single-vertex bistable origami mechanism. *Smart Mater. Struct.* 23 (9), 094009.
- Huang, H., Hagman, A., Nygå rds, M., 2014. Quasi static analysis of creasing and folding for three paperboards. *Mech. Mater.* 69 (1), 1134.
- Huffman, D.A., 1976. Curvature and creases: a primer on paper. *IEEE Trans. Comput. C-25*, 1010–1019.
- Hull, T.C., 2012. *Project Origami: Activities for Exploring Mathematics*, 2nd ed. CRC Press.
- Kumar, P., Pellegrino, S., 2000. Computation of kinematic paths and bifurcation points. *Int. J. Solids Struct.* 37 (46–47), 7003–7027.
- Lechenault, F., Thiria, B., Adda-Bedia, M., 2014. Mechanical response of a creased sheet. *Phys. Rev. Lett.* 112 (24), 244301.
- Leon, S.E., Lages, E.N., de Araújo, C.N., Paulino, G.H., 2014. On the effect of constraint parameters on the generalized displacement control method. *Mech. Res. Commun.* 56, 123–129.
- Liu, K., Paulino, G.H., 2016. MERLIN: a MATLAB implementation to capture highly nonlinear behavior of origami. In: Kawaguchi, K., Mohsaki, T. (Eds.), *Proceedings of IASS Symposium on Spatial Structures in the 21st Century*. Takeuchi, Tokyo, Japan.
- Liu, K., Paulino, G. H., 2017. *Nonlinear mechanics of non-rigid origami: an efficient computational approach*, submitted.
- Lobkovsky, A.E., Gentges, S., Li, H., Morse, D., Witten, T.A., 1995. Scaling properties of stretching ridges in a crumpled elastic sheet. *Science* 270 (5241), 1482–1485.
- Lv, C., Krishnaraju, D., Konjevod, G., Yu, H., Jiang, H., 2014. Origami based mechanical metamaterials. *Sci. Rep.* 4, 5979–5981.
- Marras, A.E., Zhou, L., Su, H.-J., Castro, C.E., 2015. Programmable motion of DNA origami mechanisms. *Proc. Natl. Acad. Sci. USA* 112 (3), 713–718.
- McGuire, W., Gallagher, R.H., Ziemian, R.D., 2000. *Matrix Structural Analysis*, 2nd ed. John Wiley and Sons, inc.
- Mentrasti, L., Cannella, F., Pupilli, M., Dai, J.S., 2013. Large bending behavior of creased paperboard. i. Experimental investigations. *Int. J. Solids Struct.* 50 (20–21), 3089–3096.
- Mentrasti, L., Cannella, F., Pupilli, M., Dai, J.S., 2013b. Large bending behavior of creased paperboard. II. Structural analysis. *Int. J. Solids Struct.* 50 (20–21), 3097–3105.
- Miura, K., 1972. Zeta-core Sandwich – Its Concept and Realization. Report No.480. Institute of Space and Aeronautical Science, University of Tokyo
- Nagasawa, S., Endo, R., Fukuzawa, Y., Uchino, S., Katayama, I., 2008. Creasing characteristic of aluminum foil coated paperboard. *J. Mater. Process. Technol.* 201 (1–3), 401–407.
- Nagasawa, S., Fukuzawa, Y., Yamaguchi, D., Nagae, S., Katayama, I., Yoshizawa, A., 2001. Deformation characteristics on creasing of paperboard under shallow indentation. In: Ravi-Chandar, K., Karihaloo, B.L., Kishi, T., Ritchie, R.O., Yokobori Jr., A.T., Yokobori, T. (Eds.), *Proc. of 10th Int. Conf. Fracture (Advances in Fracture Research)*. Elsevier Science, Amsterdam. ICF10-0202OR
- Nagasawa, S., Fukuzawa, Y., Yamaguchi, T., Tsukatani, S., Katayama, I., 2003. Effect of crease depth and crease deviation on folding deformation characteristics of coated paperboard. *J. Mater. Proc. Technol.* 140 (1–3), 157–162.
- Narain, R., Pfaff, T., O'Brien, J.F., 2013. Folding and crumpling of adaptive sheets. *ACM Trans. Graph.* 32 (4).
- Nilson, A. H., Sexsmith, R. G., Fennes, S. J., Ingraffea, A. R., Baker, B., McCafferty, P. S., 2013. Remembering William Bill McGuire. *Transcripts of Tributes to the Memorial Gathering on September 7, 2013, Cornell University, 1920–2013*.
- Peraza-Hernandez, E.A., Hartl, D.J., Akleman, E., Lagoudas, D.C., 2016. Modeling and analysis of origami structures with smooth folds. *Comput. Aided Des.* 78, 93–106.
- Phaal, R., Calladine, C.R., 1992. A simple class of finite elements for plate and shell problems. I: elements for beams and thin flat plates. *Int. J. Numer. Methods Eng.* 35 (5), 955–977.
- Phaal, R., Calladine, C.R., 1992b. A simple class of finite elements for plate and shell problems. II: an element for thin shells, with only translational degrees of freedom. *Int. J. Numer. Methods Eng.* 35 (5), 979–996.
- Pradier, C., Cavoret, J., Dureisseix, D., Jean-Mistral, C., Ville, F., 2016. An experimental study and model determination of the mechanical stiffness of paper folds. *J. Mech. Des.* 138 (4), 041401.
- Qiu, C., Zhang, K., Dai, J.S., 2016. Repelling-screw based force analysis of origami mechanisms. *J. Mech. Rob.* 8 (3), 031001.
- Resch, R., Christiansen, H.N., 1970. Kinematic folded plate system. In: Krapfenbauer, R. (Ed.), *Proceedings of IASS Symposium on Folded Plates and Prismatic Structures*. IASS, Vienna, Austria.
- Saito, K., Tsukahara, A., Okabe, Y., 2015. New deployable structures based on an elastic origami model. *J. Mech. Des.* 137 (2), 021402–021402-5
- Schenk, M., 2011. *Folded shell structures*. Ph.D. thesis. Univ of Cambridge, Cambridge, United Kingdom.
- Schenk, M., Guest, S.D., 2011. Origami folding: a structural engineering approach. In: Wang-Iverson, P., Lang, R., Yim, M. (Eds.), *Origami 5, Proc. 5th Int. Meeting on Origami Science, Mathematics, and Education*, pp. 293–305.
- Schenk, M., Guest, S.D., 2013. Geometry of miura-folded metamaterials. *Proc. Natl. Acad. Sci. USA* 110 (9), 3276–3281.
- Schenk, M., Guest, S.D., McShane, G.J., 2014. Novel stacked folded cores for blast-resistant sandwich panels. *Int. J. Solids Struct.* 51 (25–26), 4196–4212.
- Silverberg, J.L., Evans, A.A., McLeod, L., Hayward, R.C., Hull, T., Santangelo, C.D., Cohen, I., 2014. Using origami design principles to fold reprogrammable mechanical metamaterials. *Science* 345, 647–650.
- Silverberg, J.L., Na, J.-H., Evans, A.A., Liu, B., Hull, T.C., Santangelo, C.D., Lang, R.J., Hayward, R.C., Cohen, I., 2015. Origami structures with a critical transition to bistability arising from hidden degrees of freedom. *Nat. Mater.* 14 (4), 389–393.
- Tachi, T., 2009. Simulation of rigid origami. In: Lang, R.J. (Ed.), *Origami 4, Proc. 5th Int. Meeting on Origami Science, Mathematics, and Education*. CRC, pp. 175–187.
- Tachi, T., 2009b. Generalization of rigid foldable quadrilateral mesh origami. In: *Proc. Int. Assoc. Shell Spatial Struct. (Valencia, Spain)*, pp. 2287–2294.
- Tachi, T., 2009c. One-DOF cylindrical deployable structures with rigid quadrilateral panels. In: *Proc. Int. Assoc. Shell Spatial Struct. (Valencia, Spain)*, pp. 2295–2305.
- Tachi, T., Hull, T.C., 2016. Self-folability of rigid origami. In: *Proc. ASME 2016 IDETC/CIE (Charlotte, NC)*. 60546
- Tachi, T., Miura, K., 2012. Rigid-foldable cylinders and cells. *J. Int. Assoc. Shell Spatial Struct.* 53, 217–226.
- Waitukaitis, S., Menaat, R., Chen, B.-g., vanHecke, M., 2015. Origami multistability: from single vertices to metasheets. *Phys. Rev. Lett.* 114 (5), 055503
- Wei, Z.Y., Guo, Z.V., Dudte, L., Liang, H.Y., Mahadevan, L., 2013. Geometric mechanics of periodic pleated origami. *Phys. Rev. Lett.* 110 (21), 215501
- Witten, T.A., 2007. Stress focusing in elastic sheets. *Rev. Mod. Phys.* 79 (2), 643–675.
- Wriggers, P., 2008. *Nonlinear Finite Element Methods*. Springer.
- Xi, Z., Lien, J.-M., 2015. Folding and unfolding origami tessellation by reusing folding path. In: *IEEE Int. Conf. Robotics and Automation (ICRA)*, May 2015.
- Xie, R., Chen, Y., Gattas, J.M., 2015. Parametrisation and application of cube and egg-box-type folded geometries. *Int. J. Space Struct.* 30 (2), 99–110.
- Yang, N., Silverberg, J.L., 2015. Decoupling local mechanics from large-scale structure in modular metamaterials. *Proc. Natl. Acad. Sci. USA* 114 (14), 3590–3595.
- Yasuda, H., Yein, T., Tachi, T., Miura, K., Taya, M., 2013. Folding behavior of Tachi-Miura polyhedron bellows. *Proc. R. Soc. A* 469 (2159), 20130351